The Astrophysical Journal, 675:49–70, 2008 March 1

HIGH-REDSHIFT QSOs IN THE SWIRE SURVEY AND THE $z\sim3$ QSO LUMINOSITY FUNCTION[1]

Brian Siana,[2,3] Maria del Carmen Polletta,[3] Harding E. Smith,[3] Carol J. Lonsdale,[4] Eduardo Gonzalez-Solares,[5] Duncan Farrah,[6] Tom S. R. Babbedge,[7] Michael Rowan-Robinson,[7] Jason Surace,[2] David Shupe,[2] Fan Fang,[2] Alberto Franceschini,[8] and Seb Oliver[9]

Received 2006 April 11; accepted 2007 October 31

ABSTRACT

We use a simple optical/infrared (IR) photometric selection of high-redshift QSOs that identifies a Lyman break in the optical photometry and requires a red IR color to distinguish QSOs from common interlopers. The search yields 100 $z \sim 3$ (U-dropout) QSO candidates with $19 < r' < 22$ over 11.7 deg^2 in the ELAIS-N1 (EN1) and ELAIS-N2 (EN2) fields of the *Spitzer* Wide-area Infrared Extragalactic (SWIRE) Legacy Survey. The $z \sim 3$ selection is reliable, with spectroscopic follow-up of 10 candidates confirming that they are all QSOs at $2.83 < z < 3.44$. We find that our $z \sim 4$ (g'-dropout) sample suffers from both unreliability and incompleteness but present seven previously unidentified QSOs at $3.50 < z < 3.89$. Detailed simulations show our $z \sim 3$ completeness to be $\sim$80%–90% from $3.0 < z < 3.5$, significantly better than the $\sim$30%–80% completeness of the SDSS at these redshifts. The resulting luminosity function extends 2 mag fainter than SDSS and has a faint-end slope of $\beta = -1.42 \pm 0.15$, consistent with values measured at lower redshift. Therefore, we see no evidence for evolution of the faint-end slope of the QSO luminosity function. Including the SDSS QSO sample, we have now directly measured the space density of QSOs responsible for $\sim$70% of the QSO UV luminosity density at $z \sim 3$. We derive a maximum rate of H I photoionization from QSOs at $z \sim 3.2$, $\Gamma = 4.8 \times 10^{-13}$ s^{-1}, about half of the total rate inferred through studies of the Lyα forest. Therefore, star-forming galaxies and QSOs must contribute comparably to the photoionization of H I in the intergalactic medium at $z \sim 3$.

Subject headings: intergalactic medium — quasars: general

Online material: machine-readable table

1. INTRODUCTION

The QSO luminosity function (QLF) is an observable constraint on models of galaxy formation and the corresponding growth of supermassive black holes (SMBHs; e.g., Small & Blandford 1992; Kauffmann & Haehnelt 2000; Haiman & Menou 2000). These models are useful in interpreting observed phenomena, such as the relation between a galaxy's black hole mass and bulge luminosity (Kormendy & Richstone 1995; Magorrian et al. 1998), as well as inferring specifics of QSO activity, such as initial black hole mass functions, QSO light curves, and accretion rates (see, e.g., Hopkins et al. 2006).

In addition to galaxy formation models, the QLF can be used to derive the QSOs' contribution to H I and He II reionization. QSOs are responsible for He II reionization at $z \sim 3$ (Jakobsen et al. 1994; Reimers et al. 1997; Hogan et al. 1997; Sokasian et al. 2002) and are presumed to have a negligible contribution to the H I reionization at $z \sim 6$ (Madau et al. 1999). However, both of these claims require assumptions about the faint-end slope of the QLF, as this has not been measured accurately at $z > 2$.

The first QLFs demonstrated a rapid increase in space densities toward higher redshift (Schmidt 1968; Schmidt & Green 1983). Deeper surveys, which primarily identified QSOs by their "UV excess,"[10] found that the faint end of the QLF was shallower than the bright end (Boyle et al. 1988; Heisler & Ostriker 1988; Koo & Kron 1988; Hartwick & Schade 1990). Recent large surveys, most notably the 2dF Quasar Redshift Survey (2QZ; Boyle et al. 2000; Croom et al. 2004), have found thousands of $z < 2.5$ QSOs. With these large samples, the QSOs have been placed into smaller bins in both luminosity and redshift, accurately constraining the shape and evolution of the QLF. The data are typically fitted to a broken power law (Boyle et al. 1988; Pei 1995)

$$\Phi(L, z) = \frac{\Phi(L^*)/L^*}{(L/L^*)^{-\alpha} + (L/L^*)^{-\beta}}, \quad (1)$$

with the break at L^* and a bright-end slope, α, steeper than the faint-end slope, β. The QLF evolution with redshift is consistent with pure luminosity evolution (PLE; Marshall et al. 1983; Marshall 1985; Boyle et al. 1988, 2000; Hartwick & Schade 1990; Croom et al. 2004; Richards et al. 2005). That is, the evolution can be parameterized by a shift in the luminosity of the break, $L^*(z)$, without any change in its shape. Recently, the 2dF-SDSS LRG and QSO Survey (2SLAQ; Richards et al. 2005) has extended

[1] Some of the data presented herein were obtained at the W. M. Keck Observatory, which is operated as a scientific partnership among the California Institute of Technology, the University of California, and the National Aeronautics and Space Administration. The Observatory was made possible by the generous financial support of the W. M. Keck Foundation.

[2] *Spitzer* Science Center, California Institute of Technology, 220-6, Pasadena, CA 91125; bsiana@ipac.caltech.edu.

[3] Center for Astrophysics and Space Sciences, University of California, San Diego, CA 92093-0424.

[4] Infrared Processing and Analysis Center, California Institute of Technology, 100-22, Pasadena, CA 91125.

[5] Institute of Astronomy, University of Cambridge, Cambridge CB3 0HA, UK.

[6] Department of Astronomy, Cornell University, Ithaca, NY 14853.

[7] Astrophysics Group, Blackett Laboratory, Imperial College, London SW7 2BW, UK.

[8] Dipartimento di Astronomia, Universita di Padova, I-35122 Padua, Italy.

[9] Astronomy Center, University of Sussex, Falmer, Brighton BN1 9QH, UK.

[10] QSOs were most easily identified as point sources with $U - B$ colors bluer than most stars.

TABLE 1
SWIRE IR Depths from Surace et al. (2005)

Filter	Central Wavelength (μm)	Depth (μJy, 5 σ)
IRAC1	3.6	6
IRAC2	4.5	7
IRAC3	5.8	42
IRAC4	8.0	50
MIPS24	24.0	250

TABLE 2
WFS Optical Depths

Filter	Central Wavelength (Å)	Width (Å)	m_{AB}(Vega)[a]	Depth (Vega, 5 σ)
U	3560	600	0.78	24.3
g'	4857	1400	−0.09	25.2
r'	6216	1380	0.15	24.5
i'	7671	1535	0.40	23.7
Z	9100	1370	0.54	22.1

[a] Parameter m_{AB}(Vega) is the Vega-to-AB conversion factor where $m_{AB} = m_{Vega} + m_{AB}$(Vega).

the UV excess QSO search 1 mag fainter to more accurately measure the faint-end slope of the QLF out to $z = 2.1$. These deeper data, when combined with the bright-end slope from the 2QZ and 6QZ (Croom et al. 2004), fit a faint-end slope, $\beta = -1.45$, and bright-end slope, $\alpha = -3.31$, and demonstrate a roughly 40-fold increase in L^* from $z = 0$ to 2.

At high redshift, various surveys have been conducted through grism searches for UV emission lines (Schmidt et al. 1995), spectroscopic follow-up of point sources with optical colors away from the stellar main sequence (Warren et al. 1994; Kennefick et al. 1995; Fan et al. 2001), X-ray (Hasinger et al. 2005), and searches for radio-loud (Dunlop & Peacock 1990) or infrared-luminous QSOs (Brown et al. 2006). These surveys all show a precipitous decrease in space densities at $z > 3$. Early data from the Sloan Digital Sky Survey (SDSS; York et al. 2000; Fan et al. 2001) show a factor of 6 decrease in $M < -25.5$ QSOs from $z = 3.5$ to 6.0. Recent results from SDSS suggest that the bright-end slope is no longer constant at $z > 3$. Rather, it is getting shallower toward higher redshift (Richards et al. 2006a). Unfortunately, these high-redshift surveys are shallow ($i \lesssim 20$) and can only measure the bright end of the QLF at $z > 3$. Therefore, little can be said about the shape of the faint end of the high-z QLF or its integrated properties (e.g., contribution to intergalactic H I, He II ionizing radiation, or black hole growth) without a census of fainter QSOs at $z > 3$.

Hunt et al. (2004, hereafter H04) searched for faint active galactic nuclei (AGNs) at $z \sim 3$ with deep Keck spectroscopy over 0.43 deg^2 and found 11 QSOs. Although limited by small numbers, the fitted faint-end slope, $\beta = -1.24 \pm 0.07$, is substantially shallower than low-redshift measurements.

X-ray–selected samples suggest a rather modest evolution in AGN space density at high z (Barger et al. 2005), or even a luminosity-dependent density evolution (LDDE) where lower luminosity AGNs peak in number density at lower redshifts than more luminous QSOs (Ueda et al. 2003; Hasinger et al. 2005).

Given the importance of the QLF in constraining models of galaxy and black hole formation, as well as the contribution of AGNs to the ionizing background, these initial indications that the QLF shape is evolving at $z > 3$ warrant deeper surveys to better constrain the high-redshift QLF.

The SWIRE Legacy Survey (Lonsdale et al. 2003), a wide-area infrared survey with deep ground-based optical data, is optimal for searches of faint QSOs at high redshift as it is deep enough to detect sub-L^* QSOs at $z \leq 4$ and covers sufficient area to detect large numbers of them. In § 3 we outline our method for creating a new QSO template spanning far-UV to mid-IR wavelengths. In § 4 we present a simple optical/IR color selection for QSOs at $z > 2.8$ and identify areas of possible contaminations or incompleteness. Our selection results are given in § 5. In § 6 the reliability of the sample is assessed through spectroscopic follow-up and analysis of the infrared colors. In § 7 we determine, through simulations and comparisons with known samples, our sample completeness as a function of redshift. In §§ 8 and 9 we present our measurement of the QLF at $z \sim 3$ and compare to previous studies. In § 10 the QSO contribution to photoionization of H I in the intergalactic medium (IGM) is computed and compared to measurements of the *total* photoionization rate.

Although many early studies of high-redshift QLFs use an Einstein–de Sitter cosmology with $H_0 = 50$ km s^{-1} Mpc^{-1}, throughout this paper we choose to use a more recent cosmology with $H_0 = 70$ km s^{-1} Mpc^{-1}, $\Omega_m = 0.3$, $\Omega_\Lambda = 0.7$ and correct other measurements accordingly. All optical magnitudes are Vega magnitudes unless stated otherwise.

2. OBSERVATIONS

The SWIRE survey covers 49 deg^2 over six fields at high Galactic latitude with minimum Galactic cirrus emission. Most of this area has now been imaged in multiple optical filters to depths $r' \lesssim 24.5$. Our analysis is conducted within the first two fields for which both optical and infrared catalogs were available, ELAIS-N1 (16^h11^m, $+55°00'$) and ELAIS-N2 (16^h37^m, $+41°02'$).

2.1. *Spitzer Infrared Data*

SWIRE is an IR imaging survey with all four bands on the Infrared Array Camera (IRAC; Fazio et al. 2004) and all three bands on the Multiband Imaging Photometer (MIPS; Rieke et al. 2004) aboard the *Spitzer Space Telescope* (Werner et al. 2004). The IR filter characteristics and SWIRE depths are summarized in Table 1. The EN1 IRAC campaign was undertaken 2004 January 14–20, and MIPS 2004 January 21–28. MIPS went into standby mode on 2004 January 25, resulting in lost AORs that were reobserved 2004 July 29. The EN2 IRAC campaign was observed 2004 July 5–6, and MIPS 2004 July 8–11.

The IRAC and MIPS photometry were measured with the SExtractor program (Bertin & Arnouts 1996) within 1.9″ and 15″ diameter apertures for IRAC and MIPS 24 μm, respectively (Surace et al. 2005). Aperture corrections were derived from measurements of composite point-spread functions from bright stars in the SWIRE fields.

2.2. *Optical Data*

The EN1 and EN2 fields were imaged as part of the Wide Field Survey (WFS; McMahon et al. 2001).[11] Images were taken with the Wide Field Camera (WFC) on the 2.5 m Isaac Newton Telescope (INT). Both EN1 and EN2 have been observed with the U, g', r', i', and Z filters over 9 deg^2 each, with 600 s exposures at each pointing in each filter. A fraction of the fields ~30% were not observed on the same night in every filter. The filter characteristics and depths are summarized in Table 2. The median

[11] See http://www.ast.cam.ac.uk/~wfcsur/.

seeing is $\sim 1.1''$ and never worse than $1.6''$. The optical coverage overlaps the *Spitzer* IR data by 7.45 and 4.29 deg^2 in EN1 and EN2, respectively (Surace et al. 2005). Data processing was done by the Cambridge Astronomical Survey Unit (CASU) and is outlined in Irwin & Lewis (2001) and Gonzalez-Solares et al. (2005).

Photometry was measured with the CASU software, requiring a source to have five contiguous pixels 1.5 σ above the background pixel noise. Detection and photometry were performed in each band separately and then matched between bands. Fluxes were measured within $2.3''$ (7 pixel) diameter apertures. Given the typical seeing of $\sim 1.1''$, these apertures contain 80%–90% of the total flux. Aperture corrections for each image were derived from bright stars within that image. Total and isophotal magnitudes were computed as well, but only aperture photometry is used in this analysis as our objects are point sources by definition. Limiting magnitudes (5 σ) for nondetections were computed from the pixel-to-pixel noise of the corresponding image. The images were not interpolated before photometry was performed and therefore do not suffer from correlated noise from projection procedures.

3. QSO TEMPLATE

Our optical QSO selection (defined in § 4.1) uses three filters that typically span the rest-frame wavelengths 700 Å $< \lambda <$ 2000 Å. For the infrared selection (see § 4.2) we use the same two filters (IRAC1 and IRAC2) for all targeted QSO redshifts, so the photometry samples a large range in the rest-frame optical to near-IR wavelengths, 5000 Å $< \lambda < 2$ μm. In order to define the expected optical/mid-IR colors of QSOs at $2.7 < z < 5.0$, we have created a QSO template that spans many decades in wavelength from the far-UV to the mid-IR.

3.1. *UV Template*

Several composite QSO spectra have been created from large QSO surveys and agree well with each other except for minor variations due to selection effects in optical color and luminosity. Vanden Berk et al. (2001) created a composite spectrum of 2200 QSOs from the SDSS spanning the wavelengths between 800 Å $< \lambda <$ 8555 Å. In order to obtain such a broad coverage in rest-frame wavelength, QSOs from a wide redshift range ($0.044 \leq z \leq 4.789$) were used. Since the UV spectrum is composed from only high-redshift QSOs, the mean continuum shortward of Lyα is artificially decreased by the large number of Lyman line absorbers at high redshift. Because the level of absorption is redshift dependent, we need a template that reflects the *intrinsic* spectral energy distribution (SED), to which we can then apply a redshift-dependent model of the H I absorption.

Telfer et al. (2002) have created a high signal-to-noise ratio (S/N) composite UV spectrum (300 Å $< \lambda <$ 1275 Å) using *Hubble Space Telescope* (*HST*) UV spectra of 77 radio-quiet QSOs. Because these data were taken in the observed UV rather than the optical, the QSOs contributing to the critical wavelength range 700 Å $< \lambda <$ 1216 Å are at lower redshift ($\langle z \rangle = 1.42$) than the SDSS QSOs (whose spectra cover the same rest-frame wavelengths at $z > 2.4$). Therefore, there is much less Lyman line and continuum absorption in this composite. Furthermore, Telfer et al. (2002) corrected for absorbers with column densities $N_{\rm H\,I} < 10^{16}$ cm^2 and statistically corrected for lower column density absorbers, resulting in a good template of the intrinsic UV spectrum of QSOs. For our UV template we have used the composite from Telfer et al. (2002) for 300 Å $< \lambda <$ 1250 Å and the SDSS composite for 2000 Å $< \lambda <$ 8555 Å. The mean of the two composites is used in the overlapping regions 1250 Å $< \lambda <$ 2000 Å, where they agree well with each other (Telfer et al. 2002).

3.2. *Optical to Mid-Infrared Template*

The SDSS composite from Vanden Berk et al. (2001) covers the optical to $\lambda <$ 8555 Å. However, at $\lambda >$ 5000 Å the composite is produced by low-z, low-luminosity AGNs and suffers significant contamination from host galaxy stellar light. Indeed, a comparison with the median broadband SED of luminous QSOs from Elvis et al. (1994), for which stellar contribution to luminosity should be small, shows a much redder continuum slope in the SDSS composite at $\lambda >$ 5000 Å. To reliably select QSOs at $2.5 < z < 6.0$ with our mid-IR photometry, a new template is needed that covers the rest frame 5000 Å $< \lambda < 2$ μm and resembles the high-luminosity ($M_{1450} < -23$) QSOs that we are targeting.

We matched the SDSS photometry of all spectroscopically confirmed QSOs in the SDSS Data Release 3 (Schneider et al. 2005) with the near-IR photometry from the Two Micron All Sky Survey (2MASS; Skrutskie et al. 2006) point-source catalog, including the 2MASS Deep Lockman Hole Catalog (Beichman et al. 2003), which goes ~ 1 mag deeper than the typical 2MASS all-sky depths. There were 8642 2MASS objects within $2''$ of the SDSS positions. To extend the template to longer wavelengths, we also matched the *Spitzer* IR photometry of the 241 SDSS QSOs in the SWIRE fields (Lockman, EN1, and EN2).

We chose to normalize the photometry at rest frame $\lambda_{\rm norm} =$ 2400 Å for three reasons. First, the $\lambda_{\rm norm}$ is easily measured with our ground-based optical/near-IR data for a broad range of redshifts, without using extrapolations and invoking assumptions about the SED spectral slope. Second, the UV flux is dominated by the AGN rather than the host galaxy stellar light. Third, this wavelength is far from any major emission lines that would significantly affect the photometry (e.g., Mg II or C III]). Only QSOs with detections in adjacent filters surrounding $\lambda_{\rm rest} =$ 2400 Å were used to minimize the interpolation of the flux to the normalization wavelength. After an F_ν(2400 Å) was calculated, only those QSOs with $M_{2400} < -24$ were used to ensure that the flux was dominated by the AGN. This also corresponds well with the minimum luminosity of QSOs in our search ($M_{1450} = -23.5$) and is ~ 1 mag brighter than the classical QSO/Seyfert demarcation. This cut in absolute magnitude left 3378 QSOs (39% of SDSS/2MASS matches), with which we made the template.

The template was made by averaging all of the flux measurements (SDSS/2MASS/SWIRE) in 1000 wavelength bins spaced logarithmically between 753 Å and 11 μm. The result is plotted in green in Figure 1 and traces well the combined template of Telfer et al. (2002) and Vanden Berk et al. (2001) in the UV. As expected, the relative UV-to-optical ratio of our template is significantly less than the Vanden Berk et al. (2001) template because our sample is subject to less contamination from the host galaxies.

Broadband photometry works well in recreating smooth, continuous SEDs, but sharp features such as emission lines and continuum breaks are convolved with the filters through which they are observed, effectively broadening the features. Deconvolution of this broadening is difficult since our photometry comes from 13 different filters (*ugrizJHK*, IRAC1–4, MIPS24). The only sharp feature at $\lambda >$ 5500 Å is the combined emission lines of Hα (λ6563) and [N II] ($\lambda\lambda$6548 and 6592). We therefore use the broadband photometry to get the shape of the underlying continuum at $\lambda >$ 5100 Å, subtract the areas affected by Hα and [N II], and interpolate the continuum along this region. We then add the Hα + [N II] profile from the Vanden Berk et al. (2001)

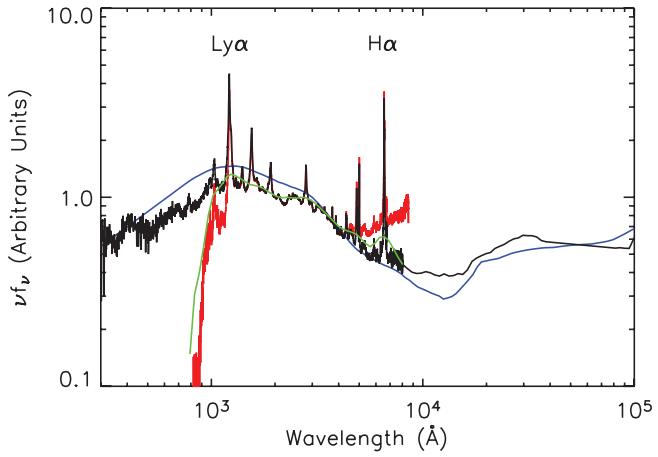

FIG. 1.—New optical/IR QSO template combined with Telfer et al. (2002) template (*black*). The broadband template at $\lambda < 8000$ Å has been replaced by the corrected Telfer/Vanden Berk template but is plotted in green to demonstrate the accuracy of the spectral slope. Also plotted for comparison are the Elvis et al. (1994) template (*blue*) and the Vanden Berk et al. (2001) SDSS composite spectrum (*red*). All templates are normalized at $\lambda = 2900$ Å.

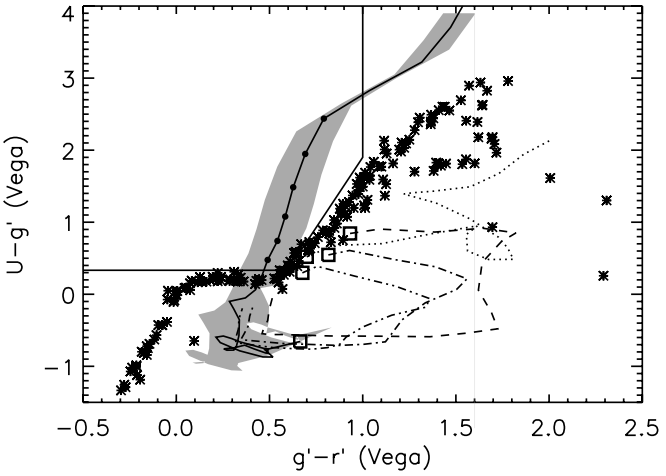

FIG. 2.—$U - g'$, $g' - r'$ color-color diagram showing the $z \sim 3$ QSO selection. The solid line is the color track of our QSO template with IGM absorption applied. The black filled circles denote the locations in redshift increments of 0.1 from $2.9 \leq z \leq 3.4$. The shaded regions denote the color space spanned by QSOs with $\pm 2\,\sigma$ deviations in the spectral slope (see Table 7). The lines are color tracks of various galaxy templates from $0 < z < 2$: Ell (age = 2 Gyr; *dotted line*), Sa (*dashed line*), Sc (*dot-dashed line*), and Sd (*double-dot–dashed line*) taken from the GRASIL library of models (Silva et al. 1998), with the boxes corresponding to their respective colors at $z = 0$. The black asterisks denote stars from the Gunn & Stryker (1983) catalog.

template (scaled to the 2400 Å continuum value to preserve the relative line strengths).

The resulting infrared QSO template is shown in Figure 1 and tabulated in Table 3. An important feature of the template is the minimum at $\lambda \sim 1$ μm and the monotonic rise (in νf_ν) toward longer wavelengths. This is produced by hot dust at varying distances from the central engine (Barvainis 1987). The minimum at $\lambda \sim 1$ μm has been shown to be prevalent in QSO SEDs (Sanders et al. 1989) and is attributed to sublimation of dust grains at $T \gtrsim 1500$ K (Barvainis 1987).

Another important aspect of this new template is the increased equivalent width (W) of Hα + [N II]. Vanden Berk et al. (2001) derived a combined W(Hα + [N II]) = 197 Å from their composite spectrum. Since the relative stellar contribution has been removed in our template, we now have W(Hα + [N II]) $\sim$ 340 Å, more than 70% higher. This proves to be important at $z \sim 4$ when Hα redshifts into the mid-IR and significantly affects the IRAC colors.

Finally, we point out that our broadband template is significantly redder than the Elvis et al. (1994) template, with the ratio of far-UV to near-IR nearly a factor of 2 larger in the latter. This is not surprising since their sample was selected in the soft (0.3–2.0 keV) and "ultrasoft" (0.1–0.3 keV) X-ray bands. Also, their sample is composed of more luminous QSOs, which are known to have bluer UV–optical colors than fainter QSOs (Richards et al. 2006b).

TABLE 3

THE BROADBAND OPTICAL/IR TEMPLATE COMBINED WITH THE TELFER ET AL. (2002)/VANDEN BERK ET AL. (2001) COMPOSITE SPECTRA

λ (μm)	f_λ
0.0302	2.250
0.0303	4.086
0.0304	6.034
0.0305	5.841
0.0306	6.000

NOTES.—Table 3 is published in its entirety in the electronic edition of the *Astrophysical Journal*. A portion is shown here for guidance regarding its form and content.

4. HIGH-REDSHIFT QSO SELECTION

In this section we define $z > 3$ QSO selection criteria requiring only three optical bands and the two most sensitive imaging bands on the *Spitzer Space Telescope* (IRAC1 and IRAC2) and assess its efficacy. The method consists of an optical color selection to identify a Lyman break in the rest-frame UV, thereby isolating QSOs to a narrow redshift range (i.e., $z \sim 3$ for U-band dropouts). In addition, we also require a red *Spitzer* IR color to eliminate typical contaminants in Lyman break galaxy (LBG) surveys (stars and low-z galaxies).

4.1. *Optical Selection*

The space density of neutral hydrogen (H I) absorbers increases rapidly with redshift (Bechtold 1994; Weymann et al. 1998). There are hundreds of absorbers with $N_{\rm H\,I} > 10^{12}$ cm^{-2} along any line of sight (LOS) to galaxies with $z > 2$, resulting in Lyman line absorption, or "blanketing," of the source's continuum at $\lambda_{\rm rest} < 1216$ Å. In addition, Lyman continuum absorption by the absorbers significantly decreases the observed flux at $\lambda_{\rm rest} < 912$ Å. At $z \geq 2.5$, these features redshift into the bluest filter accessible to ground-based telescopes (U band) and can be identified by a flux decrement at wavelengths shortward of an otherwise blue continuum. This method, known as the Lyman break technique, has been used extensively to search for both QSOs and galaxies at $z > 3$ (Irwin et al. 1991; Steidel et al. 1996; Madau et al. 1996).

We use the Madau (1995) prescription for the H I opacity evolution to determine average QSO colors as a function of redshift. Figure 2 shows the $U - g'$, $g' - r'$ color track of our QSO template as it is redshifted and the H I absorption is applied. At $z = 2.3$ the Lyman break redshifts into the U filter, resulting in redder $U - g'$ colors, thereby causing the QSO to move away from the locus of blue, low-redshift QSOs. At $z \gtrsim 2.8$ the QSO moves away from the optical color space of main-sequence stars and into color space unoccupied by typical stars or galaxies. We can

TABLE 4
Optical Selection Criteria

Sample	Color Criteria (Vega)
$z \sim 3$	$U - g' \geq 0.33$
	$g' - r' \leq 1.0$
	$U - g' \geq 3.9(g' - r') - 2.0$
$z \sim 4$	$g' - r' \geq 1.241$
	$r' - i' \leq 1.146$
	$g' - r' \geq 2.178(r' - i') + 0.09$

therefore search for QSOs in this color space while minimizing contamination.

Our color selection for both the $z \sim 3$ and $z \sim 4$ sample, defined in Table 4 and shown in Figures 2 and 3, was defined to select QSOs with $\lesssim 2\ \sigma$ deviation in spectral slope (see § 7.3.1). As we expect to eliminate stars and low-z galaxies from our sample with an additional IR selection, we are able to use a color cut that is much broader (and closer to the stellar locus) than optical-only surveys such as SDSS.

In addition to these color criteria, a candidate QSO is required to be unresolved in images taken through the two redder filters (e.g., g' and r' for $z \sim 3$ selection). This minimizes contamination from low-z galaxies. Our sample is limited to objects brighter than $r' < 22$, corresponding to S/N ≥ 20 in both g' and r'. Therefore, we have sufficient sensitivity to detect significant deviations from a point source (e.g., FWHM $> 0.5''$).

4.2. *Infrared Selection*

As seen in Figures 2 and 3, we expect some contamination from stars in both our U-dropout and g'-dropout samples. Fortunately, the mid IR SEDs of stars are very blue in color as they lie on the Rayleigh-Jeans side of the blackbody spectrum, whereas QSO SEDs are red, rising (in νf_ν) toward longer wavelengths as seen in Figure 1. Many groups have proven *Spitzer*'s ability to select AGNs with IRAC colors (Lacy et al. 2004; Stern et al. 2005; Hatziminaoglou et al. 2005). In Figure 4 we plot the IRAC colors of all point sources with $r' < 22$. There are two clear loci of points. The objects with blue IR colors (*lower left*) are stars and those with red IR colors (*upper right*) are AGNs. Both Lacy et al. (2004) and Stern et al. (2005) use all four IRAC bands to select AGNs, but Figure 4 shows that the IRAC1-IRAC2 is a robust discriminator of AGNs from stars when a point-source criterion is also used. Also, we seek an IR selection using only IRAC channels 1 and 2 since they are $\sim$2 mag more sensitive than channels 3 and 4 given the same exposure time (see Table 1). Therefore, we apply the IR color cut of

$$[3.6] - [4.5] > -0.15 \quad \text{(AB)} \tag{2}$$

in addition to our optical selection to remove stars from our sample. Here [3.6] and [4.5] are AB magnitudes at 3.6 and 4.5 μm, respectively, corresponding to $f_\nu(4.5\ \mu\text{m})/f_\nu(3.6\ \mu\text{m}) > 0.87$.

Finally, we search only sources with $f_\nu(4.5\ \mu\text{m}) \geq 10\ \mu$Jy ($\sim 7\ \sigma$) so that Poisson errors in the flux measurement are minimized, thereby decreasing the risk of contamination from sources with large errors in IRAC colors. We see in § 7.1 that this matches well our $r' < 22$ optical cut.

In addition to stellar contamination, some low-redshift galaxies may also meet our optical color criteria. This is due to the Balmer or 4000 Å break being mistaken for a U- or g'-dropout at $z < 0.1$ and $0.1 < z < 0.5$, respectively. Our point-source criterion will remove the lowest redshift galaxies as they will have large angular diameters, but our optical images may not resolve the most compact galaxies at $0.3 < z < 0.5$. Therefore, we expect to see some contamination from galaxies within this redshift range in the g'-dropout sample. In Figure 5, the [3.6] − [4.5] colors of our QSO and galaxy templates are plotted versus redshift,

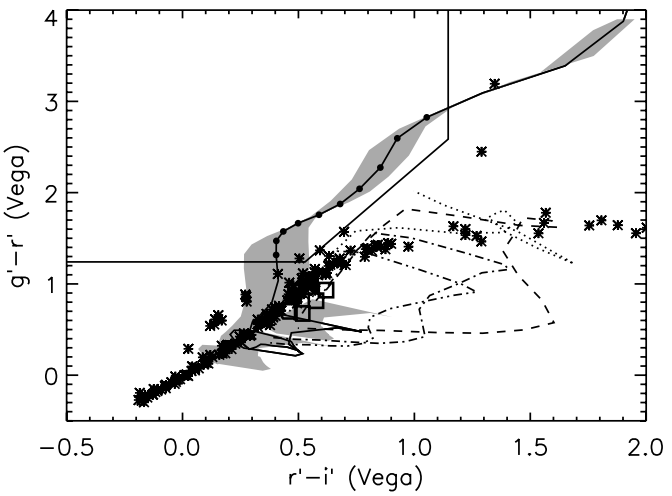

Fig. 3.—The $g' - r'$, $r' - i'$ color-color diagram showing the $z \sim 4$ QSO selection. The symbols and lines are the same as in Fig. 2.

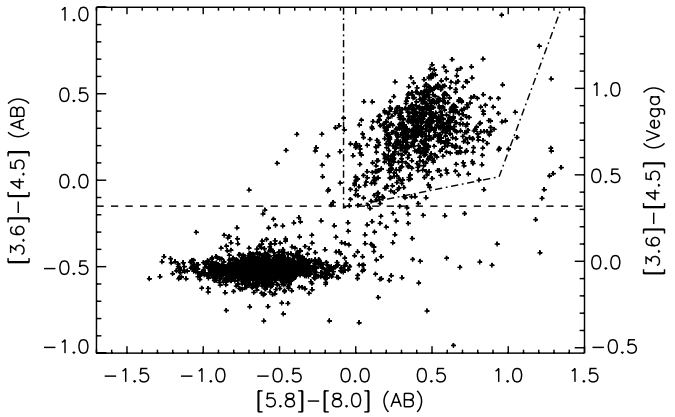

Fig. 4.—IRAC colors of point sources in ELAIS-N1 with $r' < 22$. The dot-dashed line is the Stern et al. (2005) AGN selection, and the dashed line is our selection [3.6] − [4.5] > -0.15 (AB) for demarcation of AGNs from stars.

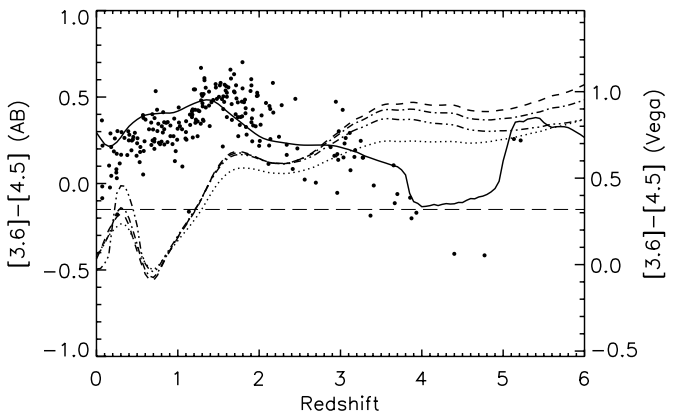

Fig. 5.—The [3.6] − [4.5] color vs. redshift. The line types are the same as in Fig. 2. Filled circles are SDSS QSOs in the SWIRE fields. The lighter, long-dashed line is our IRAC color selection, [3.6] − [4.5] > -0.15 (AB).

as well as the IR colors of SDSS QSOs in the SWIRE fields. Unfortunately, many galaxies that may contaminate our g'-dropout optical selection (i.e., $0.3 < z < 0.5$) are expected to meet our IR color selection. This is due primarily to the presence of strong 3.3 μm PAH emission in star-forming galaxies (Imanishi & Dudley 2000). Therefore, we expect some contamination from $z \sim 0.4$ galaxies within our $z \sim 4$ QSO sample.

In Figure 5 we can see that both our QSO template and all but three of the SDSS QSOs remain above our IRAC color cut for $0 < z < 3.9$, including the 18 of 19 SDSS QSOs in the targeted redshift range for U-dropouts. However, the QSO template dips close to our IR color cut between $3.8 < z < 4.8$, as do four of the five SDSS QSOs in this redshift range. This is partly due to the change to bluer slope at $\lambda < 1.5$ μm but is caused primarily by Hα redshifting into IRAC1. At these redshifts the Hα equivalent width is $W(\mathrm{H}\alpha) \sim 0.15$ μm and the IRAC1 filter width is 0.7 μm. Therefore, the Hα flux causes the $[3.6] - [4.5]$ color to decrease by $\sim$0.2 mag. As a result, the g'-dropout selection may suffer from significant incompleteness between $3.9 < z < 4.5$ (in addition to the unreliability discussed above).

4.3. *Selection Summary*

The selection is summarized as follows:

1. Point source brighter than $r' < 22$ ($i' < 21.5$ for $z \sim 4$ sample) to ensure proper morphological characterization and bright enough to determine a large $U - g'$ ($g' - r'$) limit.
2. IRAC2 > 10 μJy to ensure high S/N needed for accurate mid-IR colors.
3. Optical colors that identify a Lyman break in the continuum (see Table 4).
4. Red mid-IR color ($[3.6] - [4.5] > -0.15$) to remove interlopers.

5. RESULTS

We performed our search in the EN1 and EN2 SWIRE fields, covering 11.7 deg^2 with both optical and IR coverage. We found 100 $z \sim 3$ and 26 $z \sim 4$ QSO candidates that meet both our optical and IR criteria. The $z \sim 3$ candidates in EN1 and EN2 and their optical/infrared photometric data are listed in Table 5. The optical colors of the $z \sim 3$ sample are plotted in Figure 6 along with the colors of all other point sources with $r' < 22$. We show that the $z \sim 4$ sample suffers from significant contamination and therefore do not list them. In § 6 we assess the reliability of our sample through spectroscopic follow-up. In § 7 we assess the completeness through Monte Carlo simulations and derive effective volumes for use in computing the luminosity function.

6. RELIABILITY

6.1. *Spectroscopic Follow-up*

Optical spectra were obtained for 10 $z \sim 3$ and 10 $z \sim 4$ QSO candidates. Thirteen spectra for faint candidates (6 U-dropouts and 7 g'-dropouts) were obtained with the Low Resolution Imaging Spectrometer (LRIS; Oke et al. 1995) on the Keck I Telescope during the nights of 2005 March 3–4. The U-dropout sample, with the expected redshift of $z \sim 3$, has the most prominent emission lines at $\lambda < 7500$ Å. Therefore, only the blue channel (see Appendix in Steidel et al. 2004) was used for these sources with a 1.5″ wide long slit and a 300 line mm^{-1} grism blazed at 5000 Å, giving a resolution of 1.43 Å pixel^{-1} over 3300 Å $< \lambda <$ 7650 Å. For the g'-dropout sample, in order to detect the C IV (λ1549) line, we used a dichroic at 6800 Å and used both the blue and red LRIS channel. We used the same grism on the blue side and the 400 line mm^{-1} grating blazed at 8500 Å on the red side giving a blue side resolution of 1.43 Å pixel^{-1} from 3300 Å $< \lambda <$ 6800 Å and 1.86 Å pixel^{-1} from 7000 Å $< \lambda <$ 8500 Å. Total exposure times ranged from 5 to 15 minutes. Both nights were photometric with seeing of $\sim$1.2″. The spectra were flux-calibrated with observations of the standard star G1919B2B from Massey et al. (1988).

Seven additional spectra (four $z \sim 3$ and three $z \sim 4$ candidates) were obtained for brighter candidates with the COSMIC spectrograph on the 5 m Hale Telescope at Palomar Observatory on the nights of 2005 March 11–14. A 300 line mm^{-1} grism blazed at 5500 Å was used with a 1.5″ wide long slit, giving a dispersion of 3.1 Å pixel^{-1} and wavelength coverage of 3800 Å $< \lambda <$ 8500 Å. The nights were photometric with poor seeing ($\sim$2″–4″) so long exposure times of 10–60 minutes were required. The spectra were flux-calibrated with observations of the standard star G191B2B from Massey et al. (1988).

All 10 U-dropout candidates are QSOs with redshifts between $2.83 < z < 3.44$, the expected redshift range for our sample. The spectra are shown in Figure 7, exhibiting broad Lyα and C IV (λ1549) lines, and the QSOs with spectroscopic confirmation are circled in Figure 6. The six candidates observed with Keck LRIS were chosen simply in ascending order in declination in order to sample the QSOs randomly in color space. After these six were shown to be QSOs, we decided to target QSOs with extreme optical colors on the edges of our selection region as these are more likely to be interlopers or objects with spurious photometry. In our subsequent run at Palomar, four of these QSOs with extreme colors were observed: one with blue $g' - r'$ color, one with red $U - g'$ color, and two with optical colors that lie close to stellar main sequence. All four are in fact QSOs at the expected redshift.

As expected (see § 4.2), our g'-dropout sample suffers from significant contamination. Seven of 10 candidates are QSOs with $3.48 < z < 3.88$ and are displayed in Figure 8 and listed in Table 6. The other three spectra are plotted in Figure 9. Two of the contaminants are galaxies at low redshift ($z = 0.354$, 0.390) and exhibit strong breaks in the continuum at $\lambda \sim 5500$ Å. At these redshifts, the interlopers' 4000 Å break falls between the g' and r' filters. The third contaminant has a high-S/N spectrum but did not show any emission features, nor a break in the continuum as expected, so we have not identified a redshift for this object. Therefore, the reliability of our $z \sim 3$ and $z \sim 4$ QSO samples is 100% (>69% 1 σ) and 70^{+16}_{-26} %, respectively.

The spectroscopic follow-up of the g'-dropouts shows the expected incompleteness at the high-redshift end of the targeted range ($3.5 < z < 4.5$). All seven confirmed QSOs have $z < 3.9$. Beyond this redshift, Hα redshifts into IRAC1 and may cause the $[3.6] - [4.5]$ color to be bluer than our color criterion.

6.2. *Infrared Reliability*

In Figure 6 there are a few tens of point sources (out of more than 11,000) with red IRAC colors that lie within the stellar locus where we would not expect QSOs to lie (*upper right*), suggesting possible contamination where the stellar locus crosses the color space of our QSO selection. These may be red galaxies at moderate redshift, highly reddened QSOs, or stars whose IRAC colors are just redder than our color cut. Figure 10 shows that indeed there is not a distinct bimodality of IRAC colors for point sources. It is clear that there are two peaks in the distribution, but there are hundreds of sources in the valley between the two peaks. We have also plotted the IRAC color distribution of the point sources that also meet our optical color criteria. In this histogram, nearly all of the sources in the valley between the two peaks have been

TABLE 5

OPTICAL / IR PHOTOMETRY OF THE 100 $z \sim 3$ QSO CANDIDATES

Number	Name	R.A. (deg)	Decl. (deg)	z_{spec}	U (Vega)	g' (Vega)	r' (Vega)	i' (Vega)	Z (Vega)	IRAC1 (μJy)	IRAC2 (μJy)	IRAC3 (μJy)	IRAC4 (μJy)	MIPS24 (μJy)
1.....	SWIRE J155907.09+550325.5	239.77954	55.05709	...	22.08	21.37	21.42	21.17	20.86	12	20	44	46	<250
2.....	SWIRE J160123.47+553750.3	240.34778	55.63064	...	22.75	22.19	21.62	21.14	21.34	20	20	<42	<50	<250
3.....	SWIRE J160153.49+542356.6	240.47287	54.39906	...	22.15	21.37	21.56	21.01	20.36	99	100	137	138	593
4.....	SWIRE J160223.85+552012.2	240.59938	55.33673	...	21.92	21.48	21.09	20.59	19.95	28	29	50	57	336
5.....	SWIRE J160318.38+552703.2	240.82657	55.45089	...	21.51	20.95	20.39	20.01	19.63	56	83	133	225	827
6.....	SWIRE J160345.78+542337.2	240.94077	54.39367	...	20.58	20.20	19.68	19.23	19.04	12	11	<42	<50	<250
7.....	SWIRE J160422.50+535454.9	241.09373	53.91525	...	22.01	21.23	20.60	20.18	20.03	26	35	60	118	473
8.....	SWIRE J160426.31+553446.9	241.10963	55.57969	...	(23.30)	21.37	20.91	20.67	20.57	22	24	41	59	<250
9.....	SWIRE J160452.28+542758.2	241.21782	54.46617	2.98	22.17	21.15	21.30	21.13	20.86	28	34	<42	67	<250
10.....	SWIRE J160520.52+552704.6	241.33548	55.45128	3.30	22.88	20.51	20.26	20.19	20.13	48	50	66	73	461
11.....	SWIRE J160528.14+560635.6	241.36725	56.10989	...	22.88	22.21	21.78	21.52	20.67	22	21	<42	45	712
12.....	SWIRE J160606.33+550412.3	241.52638	55.07008	...	22.83	22.25	21.89	21.55	21.13	16	19	<42	35	<250
13.....	SWIRE J160617.56+541649.5	241.57318	54.28042	...	23.60	22.00	21.21	20.74	21.19	32	37	59	116	290
14.....	SWIRE J160621.18+552532.7	241.58827	55.42574	...	23.12	21.59	21.11	20.68	20.21	53	61	76	78	382
15.....	SWIRE J160637.88+535008.4	241.65784	53.83568	2.943[a]	20.63	19.79	19.47	18.95	18.75	109	169	312	739	2904
16.....	SWIRE J160654.19+554028.4	241.72578	55.67455	2.97	22.45	21.72	21.20	20.82	20.63	21	29	<42	58	306
17.....	SWIRE J160656.10+535633.4	241.73373	53.94261	...	(23.33)	21.53	21.12	20.66	20.57	32	33	<42	68	276
18.....	SWIRE J160724.00+533615.2	241.85002	53.60422	...	(23.25)	21.77	21.12	20.69	20.48	15	17	<42	45	203
19.....	SWIRE J160733.94+554428.7	241.89142	55.74130	...	21.24	20.39	19.69	19.04	18.45	112	138	228	375	995
20.....	SWIRE J160754.39+533916.6	241.97661	53.65462	3.01	23.29	22.39	21.93	21.49	21.37	20	23	<42	<50	202
21.....	SWIRE J160758.67+543137.8	241.99446	54.52716	...	21.46	20.85	20.59	20.19	19.84	44	43	<42	80	<250
22.....	SWIRE J160824.08+542003.7	242.10033	54.33435	...	22.98	22.39	21.98	21.71	21.04	17	16	<42	<50	<250
23.....	SWIRE J160850.55+545800.5	242.21063	54.96680	...	(23.34)	22.60	21.92	21.52	21.45	11	11	<42	<50	<250
24.....	SWIRE J160907.33+543329.8	242.28056	54.55827	...	22.85	21.16	20.57	20.33	20.15	30	36	49	113	443
25.....	SWIRE J160917.26+553638.2	242.32191	55.61062	...	22.85	21.33	20.96	20.64	20.21	50	62	57	87	305
26.....	SWIRE J160947.86+552542.9	242.44943	55.42857	...	20.47	19.91	19.35	19.03	18.73	71	84	82	208	690
27.....	SWIRE J161008.08+552944.2	242.53366	55.49561	...	22.56	21.73	21.46	21.17	20.92	14	14	<42	<50	<250
28.....	SWIRE J161008.34+533254.9	242.53476	53.54857	3.20	22.81	21.51	20.99	20.18	19.78	63	66	82	150	494
29.....	SWIRE J161051.96+531004.4	242.71651	53.16788	...	22.79	21.82	21.09	20.56	20.15	32	37	58	110	417
30.....	SWIRE J161115.37+534029.2	242.81406	53.67478	...	22.89	22.28	21.77	20.75	20.05	121	117	132	135	<250
31.....	SWIRE J161128.36+553409.9	242.86815	55.56943	...	(23.08)	22.35	21.70	21.34	21.27	15	24	<42	<50	<250
32.....	SWIRE J161128.47+535809.3	242.86862	53.96926	...	(23.34)	22.24	21.94	21.46	21.72	22	38	58	190	754
33.....	SWIRE J161132.10+542312.0	242.88374	54.38667	...	22.86	21.23	20.58	20.43	20.26	48	56	70	131	299
34.....	SWIRE J161142.40+533104.6	242.92667	53.51794	3.06	22.42	21.35	21.04	20.77	20.51	37	43	57	86	302
35.....	SWIRE J161202.93+532346.9	243.01221	53.39636	...	(23.12)	21.23	20.51	20.20	19.97	26	29	<42	<50	195
36.....	SWIRE J161251.98+534608.8	243.21658	53.76910	3.44	23.80	21.68	20.93	20.55	20.59	20	22	<42	<50	<250
37.....	SWIRE J161300.88+544629.6	243.25368	54.77489	...	23.27	21.75	21.74	21.09	21.73	27	38	<42	76	166
38.....	SWIRE J161311.87+542403.7	243.29944	54.40102	...	22.65	22.18	21.83	21.46	21.27	29	32	53	43	237
39.....	SWIRE J161326.39+530923.0	243.35994	53.15638	2.83	20.34	19.88	19.47	19.25	19.04	68	94	124	217	574
40.....	SWIRE J161341.27+532956.4	243.42195	53.49900	...	22.79	21.95	21.24	21.05	21.26	23	31	<42	78	<250

TABLE 5—*Continued*

Number	Name	R.A. (deg)	Decl. (deg)	z_{spec}	U (Vega)	g' (Vega)	r' (Vega)	i' (Vega)	Z (Vega)	IRAC1 (μJy)	IRAC2 (μJy)	IRAC3 (μJy)	IRAC4 (μJy)	MIPS24 (μJy)
41	SWIRE J161430.84+555133.3	243.62848	55.85926	...	22.74	21.85	21.53	21.20	21.41	22	28	48	73	208
42	SWIRE J161433.14+533249.6	243.63808	53.54710	...	21.04	20.15	19.55	19.36	19.07	112	124	151	306	1068
43	SWIRE J161442.44+554614.2	243.67683	55.77060	...	22.86	21.68	21.12	20.76	20.48	19	22	<42	56	<250
44	SWIRE J161446.30+555229.5	243.69290	55.87486	...	(23.19)	22.24	21.53	20.86	20.76	28	38	<42	107	308
45	SWIRE J161508.88+555514.6	243.78700	55.92073	...	20.55	19.71	19.29	18.92	18.78	55	75	122	301	924
46	SWIRE J161526.80+555217.4	243.86165	55.87150	...	22.50	21.96	21.33	20.66	20.19	67	78	117	237	810
47	SWIRE J161530.88+555247.1	243.87868	55.87976	...	22.91	22.37	21.97	21.49	20.75	58	58	60	<50	<250
48	SWIRE J161549.80+540834.9	243.95749	54.14304	...	(23.18)	22.25	21.84	21.66	22.05	9	11	<42	<50	<250
49	SWIRE J161626.05+535132.9	244.10854	53.85915	...	(23.42)	21.48	20.82	20.29	19.93	43	45	63	98	286
50	SWIRE J161634.24+553528.2	244.14265	55.59116	...	20.14	19.68	19.29	19.01	18.86	55	66	89	161	705
51	SWIRE J161638.27+555701.4	244.15947	55.95039	...	21.60	20.82	20.42	19.93	19.80	46	62	72	153	616
52	SWIRE J161704.50+541200.4	244.26875	54.20012	...	23.24	22.13	21.48	21.15	21.08	8	10	<42	<50	265
53	SWIRE J161719.00+540154.3	244.32916	54.03175	...	22.66	22.05	21.42	21.17	20.98	28	40	45	107	356
54	SWIRE J161735.03+543830.8	244.39594	54.64189	...	23.66	22.42	21.84	21.64	21.32	16	21	<42	44	381
55	SWIRE J161735.16+541405.9	244.39650	54.23497	...	22.68	20.08	19.57	19.22	19.11	56	64	117	185	717
56	SWIRE J161849.23+543658.3	244.70511	54.61620	...	22.37	21.91	21.53	21.28	21.13	15	17	<42	38	<250
57	SWIRE J161936.10+541701.2	244.90041	54.28368	...	20.10	19.74	20.25	20.10	19.84	195	235	329	378	1212
58	SWIRE J161959.51+551453.8	244.99796	55.24828	...	(23.29)	22.05	21.78	21.87	21.48	12	12	<42	42	283
59	SWIRE J162004.22+545023.4	245.01758	54.83984	...	22.80	20.68	20.45	20.22	20.12	45	56	104	224	989
60	SWIRE J163032.07+405733.9	247.63361	40.95943	...	21.05	20.70	20.12	19.69	19.49	11	10	<42	<50	<250
61	SWIRE J163130.11+403555.6	247.87546	40.59879	...	22.43	21.43	21.94	20.92	20.29	113	99	117	110	650
62	SWIRE J163219.12+404637.2	248.07965	40.77701	...	20.26	19.78	19.46	19.14	19.11	76	103	148	291	1032
63	SWIRE J163259.11+401056.6	248.24628	40.18239	...	22.88	22.17	21.76	21.58	21.19	20	23	<42	60	307
64	SWIRE J163340.14+404733.0	248.41725	40.79249	...	22.65	22.26	21.99	21.40	21.02	26	33	<42	<50	<250
65	SWIRE J163343.54+403739.5	248.43143	40.62764	...	20.91	20.34	19.71	19.31	19.14	36	34	<42	<50	<250
66	SWIRE J163357.79+400225.5	248.49081	40.04041	...	(23.18)	21.44	20.83	20.56	20.57	34	37	48	56	<250
67	SWIRE J163359.28+410921.1	248.49701	41.15587	...	21.52	21.17	20.81	20.42	19.93	40	44	65	108	<250
68	SWIRE J163403.26+403845.1	248.51360	40.64585	...	22.81	22.17	21.54	20.93	20.91	20	19	<42	<50	<250
69	SWIRE J163413.96+412028.3	248.55818	41.34119	...	22.44	21.41	20.92	20.54	20.53	20	26	48	98	376
70	SWIRE J163417.97+410531.9	248.57487	41.09219	...	21.12	20.25	20.17	19.60	19.48	63	73	107	201	606
71	SWIRE J163423.23+400244.0	248.59680	40.04555	...	20.89	20.56	20.04	19.52	19.40	47	69	113	252	1080
72	SWIRE J163511.20+404335.4	248.79665	40.72651	...	21.62	21.04	20.64	19.94	19.75	39	41	43	86	180
73	SWIRE J163527.24+395907.4	248.86349	39.98538	...	21.89	21.33	20.85	20.45	20.25	40	47	74	171	590
74	SWIRE J163536.67+412338.7	248.90279	41.39407	...	22.65	22.02	21.77	21.22	21.54	7	12	<42	<50	<250
75	SWIRE J163537.37+414904.2	248.90570	41.81784	...	22.23	21.00	20.55	20.17	20.14	29	36	63	126	415
76	SWIRE J163553.80+412641.9	248.97417	41.44498	...	22.90	21.96	21.31	21.03	20.60	25	32	53	87	<250
77	SWIRE J163604.98+410307.7	249.02077	41.05215	...	22.26	21.82	21.21	20.71	20.57	13	15	<42	<50	<250
78	SWIRE J163627.59+405153.2	249.11494	40.86479	...	22.54	21.16	20.65	20.18	19.99	28	38	37	137	653
79	SWIRE J163627.66+404218.8	249.11525	40.70521	...	21.68	21.20	20.63	20.19	19.98	14	14	<42	<50	<250
80	SWIRE J163631.32+412904.7	249.13049	41.48464	...	22.14	21.71	21.11	20.21	19.78	208	313	332	451	1554

TABLE 5—*Continued*

Number	Name	R.A. (deg)	Decl. (deg)	z_{spec}	U (Vega)	g' (Vega)	r' (Vega)	i' (Vega)	Z (Vega)	IRAC1 (μJy)	IRAC2 (μJy)	IRAC3 (μJy)	IRAC4 (μJy)	MIPS24 (μJy)
81	SWIRE J163657.12+412850.0	249.23801	41.48055	...	21.90	21.55	21.17	20.78	20.33	17	26	<42	58	<250
82	SWIRE J163711.53+415912.2	249.29805	41.98671	...	(23.38)	22.51	21.96	21.59	21.54	7	10	<42	<50	<250
83	SWIRE J163723.50+414757.5	249.34790	41.79930	...	22.86	21.86	21.46	21.09	21.15	19	27	69	<50	<250
84	SWIRE J163733.22+413116.4	249.38840	41.52121	...	(23.30)	21.88	21.80	21.15	21.03	14	19	<42	37	<250
85	SWIRE J163744.75+414245.6	249.43646	41.71266	...	21.17	20.64	20.10	19.52	19.46	32	38	71	151	634
86	SWIRE J163822.19+403650.9	249.59245	40.61413	...	21.94	20.97	20.66	20.40	20.40	28	28	<42	52	<250
87	SWIRE J163834.42+410014.9	249.64342	41.00415	...	22.44	21.75	21.62	21.65	21.29	13	14	35	52	264
88	SWIRE J163852.28+410923.7	249.71785	41.15657	...	22.43	22.06	21.79	20.89	20.62	56	85	108	169	476
89	SWIRE J163853.36+421433.2	249.72234	42.24255	...	20.95	20.56	20.17	20.05	20.03	95	133	209	309	1023
90	SWIRE J163916.07+414823.7	249.81694	41.80657	...	(23.27)	22.06	21.32	21.00	20.61	18	23	<42	<50	<250
91	SWIRE J163918.81+412206.3	249.82837	41.36841	...	(23.43)	20.89	20.36	19.88	19.85	43	52	84	176	441
92	SWIRE J163920.04+421745.8	249.83350	42.29605	...	22.80	21.83	21.31	21.10	20.84	32	35	<42	<50	<250
93	SWIRE J163940.71+403140.7	249.91962	40.52798	...	22.06	21.39	20.79	20.73	20.25	27	32	51	69	<250
94	SWIRE J163941.78+403909.8	249.92409	40.65273	...	22.53	22.19	21.70	21.27	20.98	8	11	<42	<50	<250
95	SWIRE J163955.93+410631.8	249.98306	41.10884	...	(23.18)	22.27	21.80	21.22	20.91	20	33	49	131	527
96	SWIRE J163956.76+404550.7	249.98650	40.76407	...	(23.16)	21.68	21.31	99.00	99.00	36	39	70	100	<250
97	SWIRE J164022.80+411548.2	250.09499	41.26338	3.064[a]	20.28	19.72	19.20	18.88	18.76	100	126	187	350	1021
98	SWIRE J164036.64+414916.2	250.15268	41.82116	...	20.81	20.46	20.28	20.02	19.69	39	51	99	128	380
99	SWIRE J164127.88+412636.4	250.36617	41.44345	...	22.34	21.71	21.26	21.00	20.62	23	26	52	60	160
100	SWIRE J164229.64+405354.3	250.62350	40.89842	...	(23.08)	22.59	21.98	21.65	21.19	56	63	55	64	285
101[b]	SWIRE J160755.85+534020.4	241.98271	53.67234	3.07	22.46	22.23	21.51	21.27	21.02	22	27	<42	54	185
102[b]	SWIRE J161046.25+532540.5	242.69270	53.42791	2.98	21.41	21.11	20.68	20.51	20.71	36	35	54	46	241

NOTES.—Spectroscopic redshifts are given when available. U-band magnitudes in parentheses are 5 σ limits. Two objects with spectroscopic confirmation were moved just outside of our color criteria (due to revised photometry) and are no longer part of our primary sample. We list these at the end of the table. Typical uncertainties are ~0.04 mag in the optical and ~10% in infrared fluxes.

[a] z_{spec} from SDSS.

[b] Revised photometry moved object outside of color criteria.

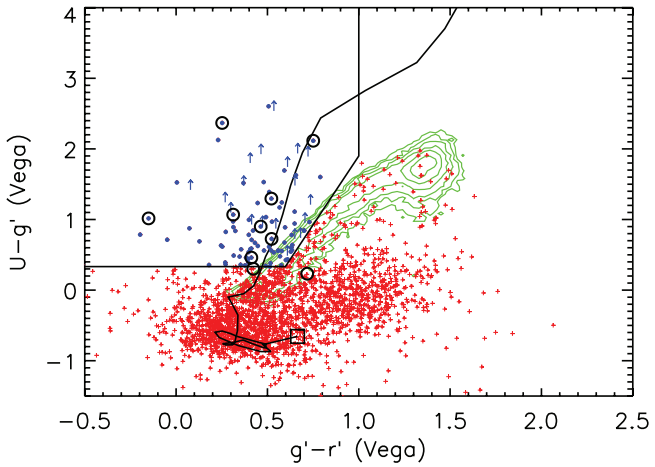

FIG. 6.—$U - g'$, $g' - r'$ optical colors of objects with $r' < 22$ and classified as point sources. The solid line is the color track of our QSO template with IGM absorption applied, and the square denotes the $z = 0$ point. The green contours denote the density (in color space) of objects categorized as stars by their blue IRAC colors ($[3.6] - [4.5] < -0.15$). Red plus signs denote point sources with red IRAC colors ($[3.6] - [4.5] > -0.15$). The blue arrows and circles also have red IRAC colors, but match the optical color criteria for $z \sim 3$ QSOs. The arrows denote upper limits where there is no detection in U. Spectroscopically confirmed candidates are circled. The photometries of two spectroscopically confirmed QSOs were revised and are therefore slightly out of our optical selection window but are still displayed here. They are both QSOs at $z \sim 3$, and their photometry is included at the end of Table 5.

removed, revealing a clear bimodality. There are two reasons for this. First, galaxies can have either red or blue IRAC colors, depending on redshift, but should not lie in the optical color space of $z \sim 3$ QSOs. Second, although a few stars may have IRAC colors redder than our cut, the stars must be either very bright or very red to be detected in IRAC channel 2 at all. Stars that lie in the $z \sim 3$ optical color space have $r' - [4.5] = 1.6$ mag (AB). Since the IRAC channel 2 flux limit corresponds to 21.4 in AB magnitudes, this means that we should not detect the stars in channel 2 unless they are brighter than $r' \lesssim 19.7$ (Vega). Indeed, in Figure 11 there are two sources at the bright end of our sample that have blue optical–IR colors and may be stars.

As mentioned in § 4.2, IRAC color selection of AGNs is robust when all four bands are used because the SEDs of most contaminants are not flat (or rising toward longer wavelengths) over such a broad wavelength range. Therefore, we can use all four IRAC fluxes, when available, to assess the reliability of our single color AGN selection. In our sample, 58% (58 of 100) of our objects are detected in all four IRAC channels, and their IRAC colors are plotted in Figure 12. Essentially all of these objects have IR colors in the expected locus of AGNs. Therefore, it appears that the contamination rate is low. However, as stellar contaminants are expected to have blue IRAC colors, we do not expect to detect the fainter interlopers in IRAC3 and IRAC4, and we cannot assess the nature of these objects. Therefore, we look at only the bright end of our sample where all sources are detected in all four bands. At $r' < 20.5$, 21 of 24 (88%) sources are detected in all four IRAC bands, and all of these have IR colors within the expected AGN locus. If we make the conservative assumption that the three nondetections (in IRAC3 and IRAC4) among the bright sample are not QSOs, then we obtain an upper limit to the contamination rate of $\lesssim 13\%$.

In summary, the point sources that match our optical color criteria have a distinct bimodal distribution in $[3.6] - [4.5]$ colors, suggesting minimal contamination from stars, except at the bright end ($r' < 20$). However, the four-band IRAC colors suggest that even the bright end of our sample has a contamination rate of less than 13%.

7. COMPLETENESS

7.1. *Infrared Completeness*

As mentioned in § 4.2, we expect our IR color cut to include nearly all QSOs at $z \sim 3$ (as seen with the SDSS QSOs). However, we must ensure that no QSOs are missing due to the $f_\nu(4.5\ \mu\text{m}) \geq 10\ \mu$Jy. Figure 11 plots the optical–IR colors of all U-dropout candidates as a function of the optical magnitudes. The locus of colors agrees well with the infrared-selected QSOs of Brown et al. (2006). Also plotted is the limit due to the IRAC2 flux cut. Except for the faintest of the six half-magnitude bins, there is no incompleteness due to nondetections in IRAC2. In the faintest bin, $21.5 < r' < 22.0$, it is possible that we miss a few of the bluest $r' - [4.5]$ QSOs, but we estimate this to be <15% (based on the $r' - [4.5]$ distribution in Fig. 11) and make no attempt to correct for it. We have also verified that increasing the counts by 15% in this bin has a negligible effect on the QLF fit.

7.2. *Morphological Completeness*

Our selection requires that the candidates be unresolved in the optical data, where typical resolution is $\sim 1.1''$. We have assumed that the QSOs are significantly brighter than their host galaxies and, even if we could detect the host galaxy, galaxies at $z > 3$ should have angular diameters less than $1''$ (Giavalisco 2002). To test this assumption, we have matched our catalogs to all of the SDSS QSOs (which do not have to meet a morphological criterion) within the EN1 and EN2 fields. Of the 58 SDSS QSOs at high redshift ($z > 1$), 57 (98%) are categorized as point sources in our optical catalogs. Therefore, we do not expect any significant incompleteness due to our point-source criterion.

7.3. *Optical Completeness*

Our color selection should be strict enough to minimize contamination, but broad enough to encompass the majority of the targeted QSOs to minimize completeness corrections. As a first-order look at completeness, we compare with the SDSS QSO sample between $3.1 < z < 3.2$ where SDSS is ~80% complete (Richards et al. 2006a). SDSS uses four colors, to look at all point sources away from the color space of stars (Richards et al. 2002). Therefore, it is possible that SDSS selects redder QSOs at $z \sim 3$, which would lie outside of our color selection. Converting SDSS to Vega magnitudes, and correcting for slight U/u' filter differences (0.06 mag correction), ~97.5% (392/402) of SDSS QSOs at $3.1 < z < 3.2$ would also be selected with our color selection. Therefore, <3% of SDSS QSOs are redder and selected with other colors in the SDSS filters.

Significant dispersion in spectral features may cause some QSOs to lie outside of our selection criteria. The most important factors affecting the optical color (and therefore the completeness) are redshift, intervening high column density H I absorbers, UV continuum slope, emission-line equivalent widths, and variability. Here we present our Monte Carlo simulations to assess the combined effects of these characteristics on our completeness as a function of magnitude and redshift. We then use this completeness to derive the effective volume of our sample as a function of apparent magnitude.

7.3.1. *Model of QSO Optical Color Distribution*

Both the UV spectral slope of the continuum α_ν, where $f_\nu \propto \nu^\alpha$, and the emission-line equivalent widths, W, can vary about the mean and cause significant dispersion in colors at any given

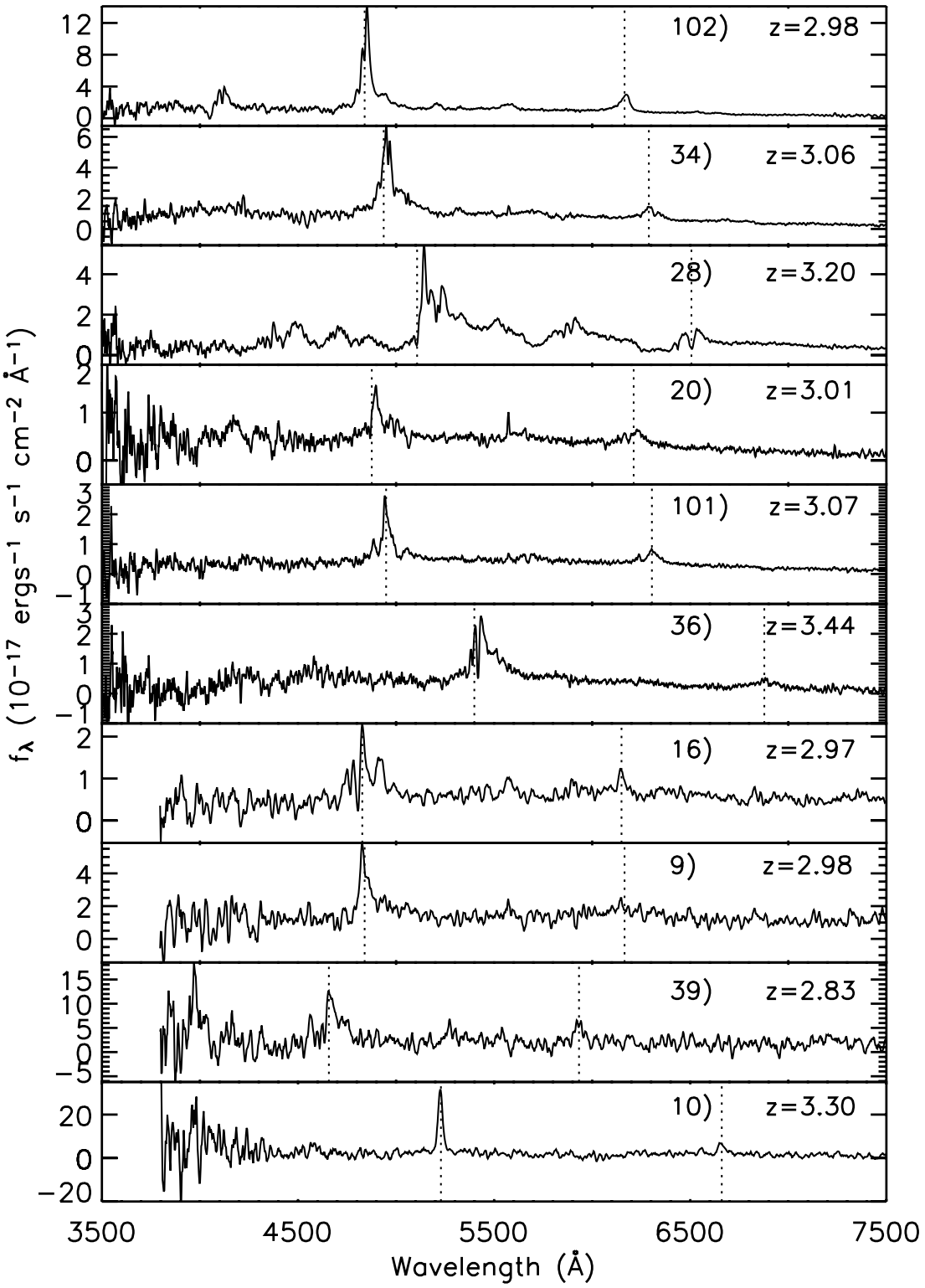

FIG. 7.—Keck/LRIS (*top six panels*) and Palomar/COSMIC (*bottom four panels*) spectra of $z \sim 3$ QSO candidates. The ID numbers from Table 5 and redshifts are given, and the Lyα and C IV lines are labeled.

redshift. The mean of the spectral slope and the equivalent widths are defined by our template spectrum and are consistent with values found by Vanden Berk et al. (2001) and H04. The distribution of these attributes is assumed to be Gaussian, with standard deviations taken from Francis (1996), and is listed in Table 7.

Along the LOS to any given QSO at high redshift there are hundreds of intervening neutral hydrogen clouds (or filaments) absorbing the UV light through Lyman line and Lyman continuum absorption. Much of this absorption is caused by the rare, high column density absorbers known as Lyman limit systems (LLSs; $N_{\rm H\,I} > 1.6 \times 10^{17}$ cm^2) and damped Lyα systems (DLAs; $N_{\rm H\,I} > 1 \times 10^{20}$ cm^2). Therefore, there is a large dispersion in LOS H I opacity at any given redshift due to the small numbers of these high column density clouds. Bershady et al. (1999) show that

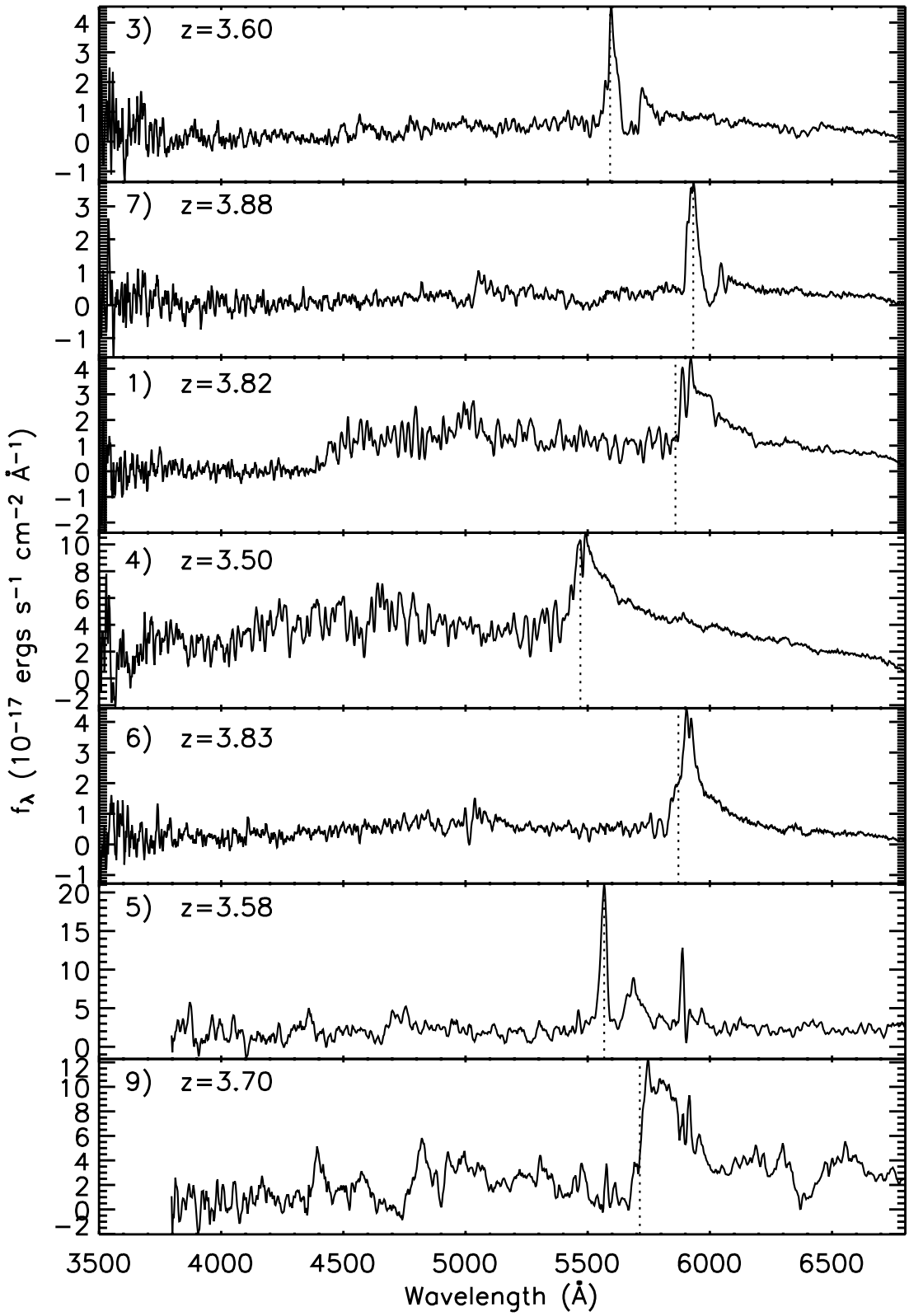

FIG. 8.—Keck/LRIS (*top five panels*) and Palomar/COSMIC (*bottom two panels*) spectra of $z \sim 4$ QSO candidates. The ID numbers from Table 6 and redshifts are given, and the Lyα line is labeled.

TABLE 6

REDSHIFTS AND OPTICAL/IR PHOTOMETRY OF THE SEVEN SPECTROSCOPICALLY CONFIRMED $z \sim 4$ (g'-DROPOUT) QSOS AND TWO SDSS QSOS IN OUR SAMPLE

Number	Name	R.A. (deg)	Decl. (deg)	z_{spec}	U (Vega)	g' (Vega)	r' (Vega)	i' (Vega)	Z (Vega)	IRAC1 (μJy)	IRAC2 (μJy)	IRAC3 (μJy)	IRAC4 (μJy)	MIPS24 (μJy)
1.....	SWIRE J160532.15+542631.0	241.38394	54.44194	3.82	23.13	22.24	20.90	20.74	20.25	32	36	65	106	387
2.....	SWIRE J160705.15+533558.7	241.77147	53.59965	3.653[a]	(22.82)	19.47	18.18	17.89	17.55	374	412	665	1392	5727
3.....	SWIRE J160907.51+535028.0	242.28130	53.84110	3.62	(22.73)	22.75	21.19	20.69	20.33	44	42	48	<50	231
4.....	SWIRE J160934.11+550015.2	242.39211	55.00421	3.52	22.44	21.30	19.79	20.18	19.85	39	40	40	60	<250
5.....	SWIRE J161143.22+553157.5	242.93008	55.53263	3.58	(23.04)	21.30	19.99	19.72	19.43	73	81	144	278	1368
6.....	SWIRE J161243.17+535827.4	243.17989	53.97428	3.83	(23.34)	22.49	21.02	20.80	20.73	22	21	36	<50	<250
7.....	SWIRE J161557.43+545915.8	243.98929	54.98772	3.880	(23.29)	23.96	21.77	21.20	21.34	36	30	<42	55	<250
8.....	SWIRE J164326.24+410343.4	250.85934	41.06205	3.873[a]	(23.11)	21.49	20.04	19.81	19.80	46	39	39	57	289
9[b]	SWIRE J104350.94+583029.3	160.96227	58.50813	3.70	...	20.95	19.43	18.97	...	105	116	189	382	1945
10[c]	SWIRE J160543.05+535829.2	241.42938	53.97477	0.354	(23.53)	23.22	21.48	20.70	20.12	27	21	<42	<50	<250
11[c]	SWIRE J161159.69+544211.3	242.99872	54.70313	0.390	22.86	22.55	20.72	20.55	19.99	57	57	<42	151	<250
12[b,d]	SWIRE J105002.88+574720.0	162.51199	57.78890	?	...	21.55	20.05	19.73	...	215	391	677	1220	3519

NOTES.—U-band magnitudes in parentheses are 5 σ limits. Typical uncertainties are $\sim$0.04 mag in the optical and $\sim$10% in infrared fluxes.

[a] z_{spec} from SDSS.

[b] Selected in the SWIRE Lockman field.

[c] Low-redshift interlopers.

[d] Could not see emission lines for redshift confirmation.

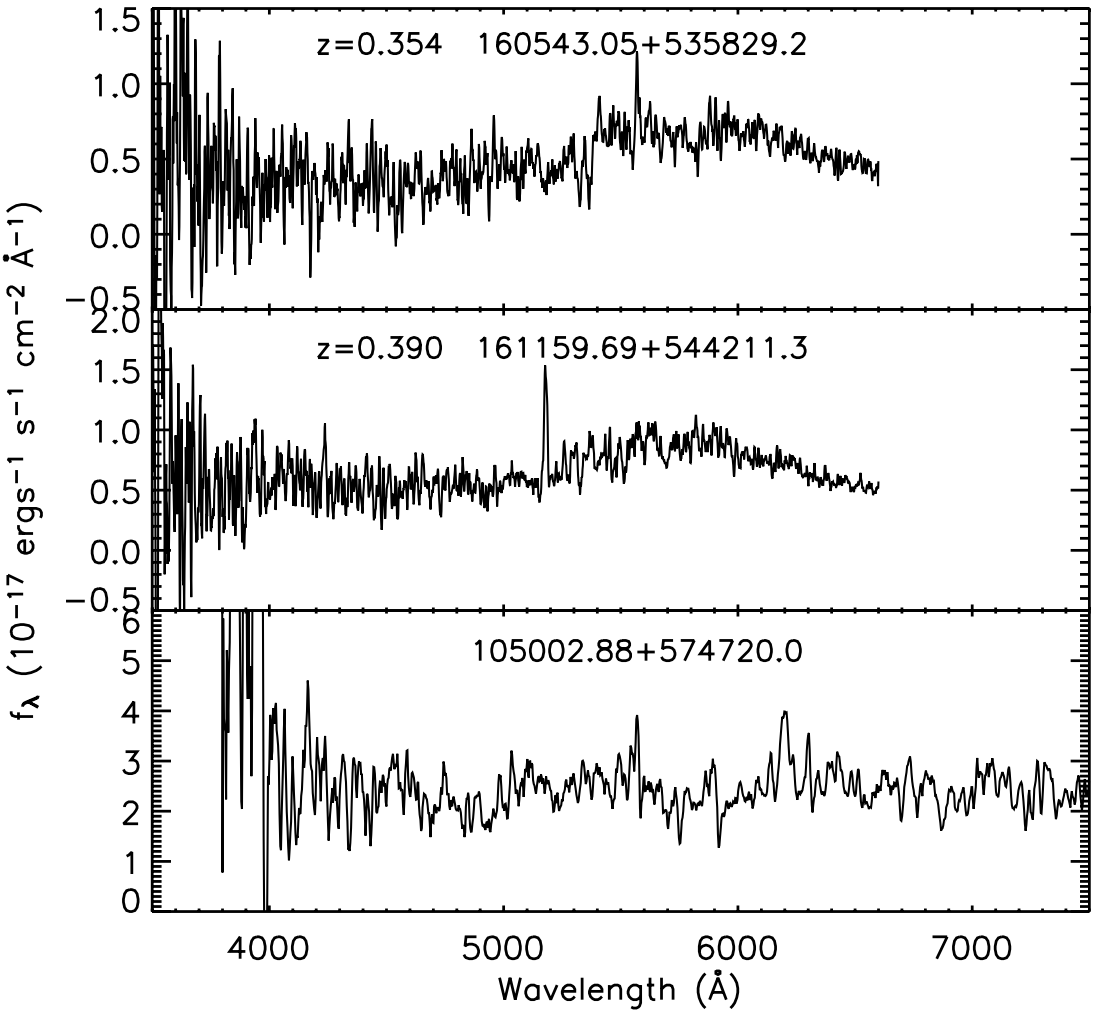

FIG. 9.—Keck/LRIS (*top and middle*) and Palomar/COSMIC (*bottom*) spectra of interlopers in the g'-dropout sample. The official SWIRE names and redshifts (if known) are labeled.

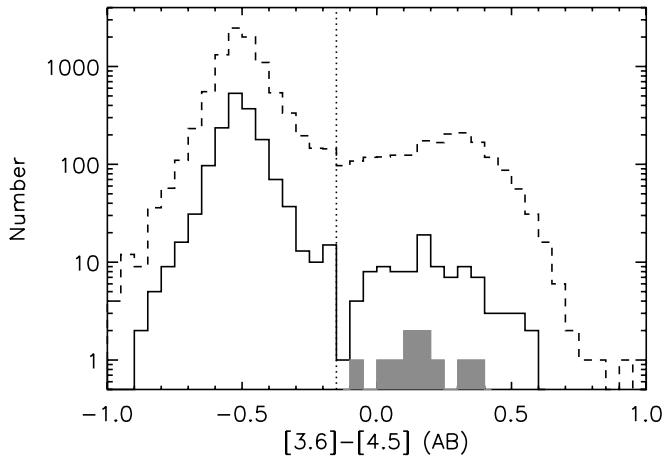

FIG. 10.—IRAC ([3.6] – [4.5]) color distribution of all point sources with $r' < 22$ in our field (*dashed line*). The solid line shows the color distribution of point sources that also meet our optical color criteria. The shaded histogram is the distribution of spectroscopically confirmed QSOs. Our QSO sample is the portion of the solid histogram to the right of the vertical dotted line.

simple analytic expressions for the mean and scatter in LOS opacity are insufficient and, therefore, Monte Carlo simulations are required to correctly represent the stochastic distributions of the absorbers.

The number density distribution of H I absorbers is typically given as a fit to a power law with redshift

$$N(z) = N_0(1+z)^{\gamma}, \tag{3}$$

and the column density distribution is given as

$$\frac{df}{dN_{\rm H\,I}} \propto N_{\rm H\,I}^{-\kappa}. \tag{4}$$

Since absorbers of different column densities are known to evolve differently (Kim et al. 1997), we have split them into four groups with differing evolution, similar to the work of Bershady et al. (1999) and Fan et al. (2001), but with updated values for DLA number densities. The parameters used are summarized in Table 8.

For each LOS, the number of LOS absorbers is selected from a Poisson distribution with the expectation value set to $\langle N \rangle$ of the population:

$$\langle N \rangle = \int_0^{z_{\rm QSO}} N(z)\, dz. \tag{5}$$

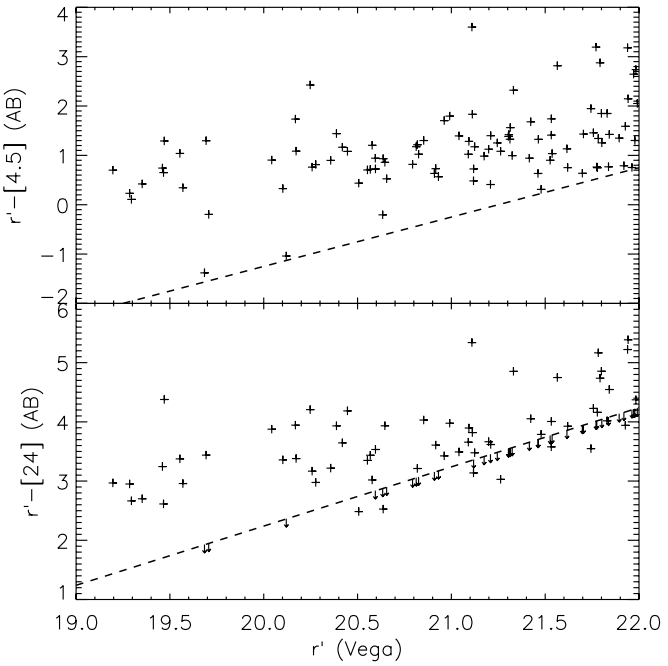

FIG. 11.—Optical–IR color distribution of the $z \sim 3$ QSO sample. The x-axis is in Vega magnitudes since our magnitude bins are defined in Vega magnitudes, and the y-axis is in AB magnitudes as it is simpler to interpret. The dashed line in the top panel denotes the $f_{4.5\,\mu\mathrm{m}} = 10\ \mu$Jy limit of our search. The dashed line in the bottom panel denotes the $f_{24\,\mu\mathrm{m}} = 250\ \mu$m completeness limit, with arrows giving upper limits from nondetections. The four QSOs with $r' - [4.5] < 0.0$ are possible interlopers.

Their redshifts and column densities are chosen randomly from the distributions in equations (3) and (4), respectively. Finally, we compute Voigt profiles with natural broadening and Doppler widths, b, from Table 8 for the first 10 Lyman lines for each absorber. We choose not to model the distribution of Doppler widths (or its evolution) as this is expected to be a small, second-order effect. Continuum absorption is applied with a scattering cross section of $\sigma_0 = 6.3 \times 10^{-18}$ cm^2 at the Lyman limit and decreasing as ν^{-3}. An example of the Lyα forest transmission for one LOS at $z = 3$ is plotted in Figure 13.

For 300 LOSs in each redshift bin of $\Delta z = 0.1$, we compute QSO spectra with spectral slopes and emission-line equivalent

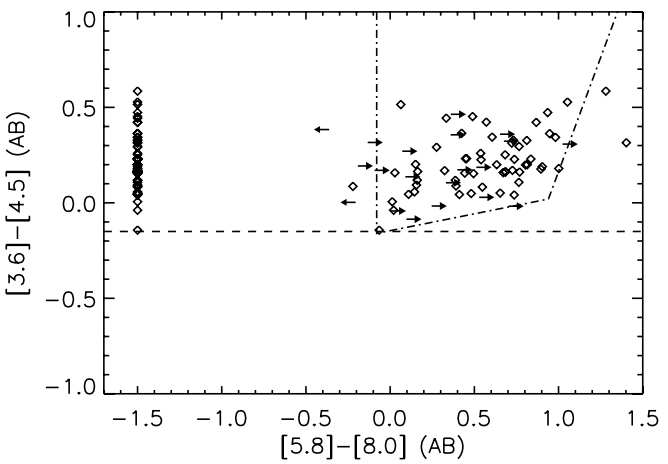

FIG. 12.—IRAC colors of the $z \sim 3$ QSO sample. The lines are as in Fig. 4. Right arrows are lower limits to the [5.8] − [8.0] color based on nondetections in IRAC3. Left arrows are upper limits to the [5.8] − [8.0] color based on nondetections in IRAC4. Nondetections in both IRAC3 and IRAC4 are plotted along the left-hand side.

TABLE 7
SPECTRAL PARAMETER ATTRIBUTE FOR OUR QSO SED MODELING

Parameter	Mean	σ
α_ν	−0.46	0.3
W(Lyα + N v) (Å)	101.7	25.

widths culled from the distributions defined in Table 8 and apply the simulated IGM absorption for that LOS.

QSOs of these luminosities and redshifts exhibit variability of order $\Delta m \sim 0.15$ mag (Vanden Berk et al. 2004). A total of 29% of our fields were observed at separate times (over 2 yr) in the U and g' filters, and 29% of our fields were observed at separate times in the g' and r' filters. We therefore add a variable offset selected from a Gaussian distribution with $\Delta m \sim 0.15$ to the computed $U - g'$ and $g' - r'$ optical colors of 30% of the simulated LOSs. The net effect of this variability is a slight ~5% decrease in completeness and a slightly broader redshift range.

After adding in variability and photometric errors, we compute the optical colors for the 300 QSOs in each redshift bin. This allows us to determine the selection completeness based on color selection alone, but the imaging depth must still be taken into consideration.

The optical magnitude limit of our QSO search, $r' = 22.0$, is set by our infrared depths and corresponds to ~20 σ detections in both g' and r'. Therefore, we do not expect any incompleteness due to nondetections in g' or r'. However, when looking for significant "U-dropouts," it is important to have deeper imaging in U relative to the bands at longer wavelengths. Otherwise, nondetections will result in upper limits in flux that cannot distinguish between a true "dropout" or a red source that is just below the detection limit. The WFS was not designed for finding U-dropouts, and the U band is generally less sensitive due to CCD quantum efficiency (QE) and poor throughput in the telescope optics. Therefore, the U-band images in the SWIRE fields are less sensitive (to all classes of object) than the g' and r' images. Furthermore, this sensitivity varies by ~0.5 mag from pointing to pointing due to changing observing conditions (seeing, air mass, lunar phase). Therefore, careful measurements of the selection completeness as a function of pointing must be assessed, along with dependencies on redshift and magnitude.

Both EN1 and EN2 are comprised of 54 $22.8' \times 11.4'$ optical pointings. For each CCD at each pointing, a 5 σ limiting magnitude is determined within our 2.3″ diameter aperture and is used as an upper limit when no object is detected.

Due to overlaps in pointings and varying observing conditions, it is nontrivial to compute the limiting magnitude for a given position on the sky. For both fields we make "depth maps" by making mosaic images of the entire field with pixel values set to the 5 σ limiting magnitude of the deepest pointing that covers that pixel. In this way, we can quickly compute the area over which we can detect an object of a given magnitude U_{test} by summing the pixels with value greater than U_{test}. These depth maps are trimmed to the area that also has *Spitzer* data. The U-band depth map for EN1 is plotted in Figure 14, showing the nonuniformity and complex structure of the coverage.

As shown in Figure 2, the bluer of the two optical colors, $(U - g')$, becomes redder as the QSO goes to higher redshift, making nondetections in U increasingly likely at higher redshift. For example, a typical $r' = 21$ QSO at $z = 2.9$ will have $g' \sim 21.5$ and $U \sim 21.8$, bright enough to be detected in all bands by our survey. However, a QSO with the same r' magnitude at $z = 3.4$ will have $g' \sim 22$ and $U \sim 24.5$, too faint to be detected in our

TABLE 8
PARAMETERS FOR THE FOUR COLUMN DENSITY RANGES USED IN THE Lyα FOREST SIMULATIONS

Name	$\log N_{\rm H\,I}(\rm cm^2)$	N_0	κ	γ	b (km s^{-1})
Lyα forest 1[a]	12–14	181.36	1.46	1.29	30
Lyα forest 2[a]	14–17.2	1.297	1.46	3.10	30
Lyman limit systems[b]	17.2–20	0.27	1.50	1.55	70
Damped Lyα systems[c]	20–22	0.055	1.78	1.11	70

[a] Kim et al. (1997).
[b] Storrie-Lombardi et al. (1994).
[c] Storrie-Lombardi & Wolfe (2000).

U images. Our upper limit in this case is insufficient in distinguishing a high-redshift QSO candidate from a low-redshift object with bluer $U - g'$.

Given our simulated spectra and our depth maps, we determine an effective completeness in the following manner. For each redshift bin, we compute $U - g'$ and $g' - r'$ colors for the 100 simulated QSOs along 100 different lines of sight. Then we compute the percentage of these QSOs that would be selected by our color criteria if our imaging was sufficiently deep. This gives us a measure of our completeness based strictly on our color criteria alone, $C_{\rm color}$. The completeness cutoff at the high-redshift end ($z \sim 3.5$) is nearly a step function since the QSO color track moves perpendicular to our color cuts and most of the dispersion in color is parallel to the color cut. At the low-redshift end ($z \sim 2.9$), the incompleteness is predominantly due to LOS variations in IGM.

Of the QSOs that meet the color criteria, the fluxes are scaled to give the desired r' magnitude in intervals of $\Delta r' = 0.25$ mag and the $g' - r'$ color is used to determine the U-band depth required to either detect this QSO or derive a lower limit to the magnitude that is high enough to put it in the color-color selection window. The percentage of QSOs with colors in our selection window that would also be selected given the U-band depth at that pixel value is denoted as $C(r', z)$, plotted in Figure 15. The effective volume of the survey can then be calculated as

$$V_{\rm eff}(r') = d\Omega \int_{z=0}^{z=\infty} C(r', z) \frac{dV}{dz}\, dz, \qquad (6)$$

where Ω is the solid angle of the survey and dV/dz is the differential comoving volume. The effective volumes and average redshifts for each half-magnitude bin are given in Table 9. To give an idea of the scales of the incompleteness corrections, the effective volume in our faintest magnitude bin $V_{\rm eff}(r' = 21.75)$ is 74% of the effective volume in our brightest bin $V_{\rm eff}(r' = 19.25)$, requiring a relatively small correction of 35% to the number counts.

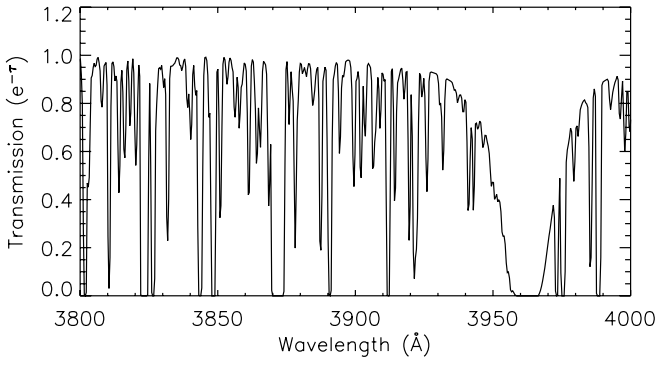

FIG. 13.—Subsection of the simulated IGM transmission ($e^{-\tau}$) curve for one simulated LOS. All absorption features are fully resolved in the simulation.

8. THE $z \sim 3$ QSO LUMINOSITY FUNCTION

Given the effective volume, $V_{\rm eff}(r')$, the comoving space density is then

$$\Phi(r') = \frac{N(r')}{V_{\rm eff}(r')} \frac{1}{w_{\rm bin}}, \qquad (7)$$

where $N(r')$ is the number of QSOs in the r' bin and $w_{\rm bin}$ is the width of the bin in magnitudes. We then convert r' to the absolute AB magnitude at 1450 Å since the r' filter covers 1450 Å over our entire redshift range and this value is generally used for high-redshift QSO studies:

$$M_{1450} = r' + r'_{\rm AB}(\rm Vega) - \rm DM(\it z = 3.2) + 2.5 \log(1 + 3.2) + \it K(\Delta z), \qquad (8)$$

where r' is the Vega magnitude listed in Table 5, $r'_{\rm AB}(\rm Vega) = 0.15$ is the Vega-to-AB conversion, DM = 47.19 is the distance modulus at $z = 3.2$, and $K(\Delta z)$ is the K-correction resulting from

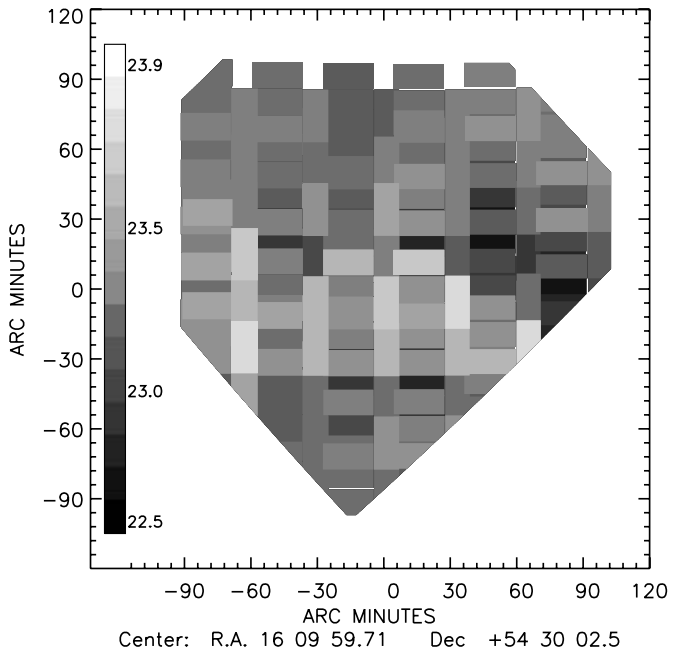

FIG. 14.—U-band depth map for EN1. The gray scale represents U magnitude limits in intervals of 0.1 mag from 22.5 to 24.0 (Vega), with most of the area between 23.0 and 23.5.

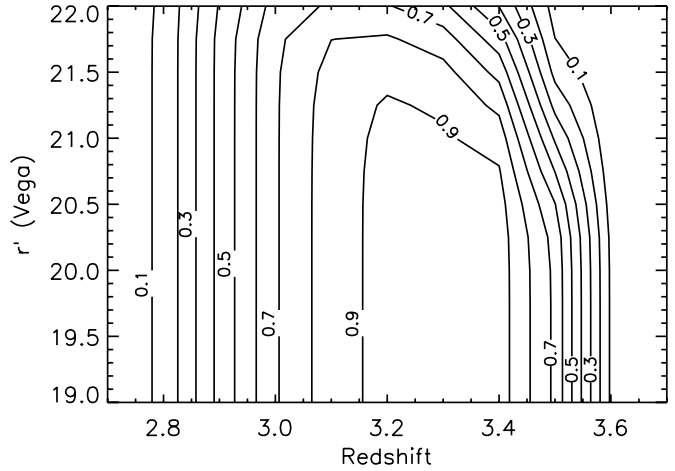

FIG. 15.— The $z \sim 3$ QSO completeness $C(r', z)$ contours as a function of apparent r' magnitude and redshift. The contours are spaced at $\Delta C = 0.1$ intervals.

shifts in redshift around $z = 3.2$. As we do not have exact redshifts for most of our QSOs, we set $K(\Delta z) = 0$, but note that this varies by ± 0.1 mag from $2.9 < z < 3.5$.

The resulting QLF at $z \sim 3.2$ is plotted in Figure 16, along with previous surveys of QSOs at these redshifts. Our measurements, while using smaller magnitude bins ($w_{\rm bin} = 0.5$ mag) than previous surveys of faint high-z QSOs, have significantly reduced error bars. The space densities at the bright end of our survey match well with the faintest bins from the SDSS (Richards et al. 2006a) and show a clear transition to a shallower slope at the faint end. We use our data in combination with the Richards et al. (2006a) SDSS results at $z \sim 3.25$ because it is the largest sample available, and its completeness corrections have been carefully determined.

We do a least-squares fit to the standard double power law given in equation (1), converted to absolute magnitudes:

$$\Phi(M_{1450}, z) = \frac{0.92\Phi\left(M^*_{1450}\right)}{10^{0.4(\alpha+1)(M_{1450}-M^*_{1450})} + 10^{0.4(\beta+1)(M_{1450}-M^*_{1450})}}. \quad (9)$$

As mentioned previously, when the error bars are reduced, the quasar luminosity function exhibits curvature over all luminosities, not just at the break (Wolf et al. 2003; Richards et al. 2005). Therefore, since both our data and the SDSS data show some curvature, and the SDSS has much smaller error bars, a least-squares fit of a double power law will force the break position (M^*) to be contained within the range of magnitudes covered by the SDSS. This produces a very steep faint-end slope and is a poor fit to our faintest bins. Of the four parameters that determine the QLF, the SDSS can only measure the bright-end slope with certainty at $z \sim 3.2$. Therefore, we also perform a fit with a fixed bright-end slope, $\alpha = -2.85$, defined by the SDSS measured relation of α with redshift at $z = 3.2$. This yields more realistic values of $M^* = -25.6$ and a faint-end slope $\beta = -1.62 \pm 0.19$, which is constrained by 4–5 bins fainter than M^*. The results of the double power-law fits are given in Table 10.

8.1. *Maximum Likelihood Fit*

In the above fit to the binned data, we assumed that all of our QSOs are at a single redshift ($z = 3.2$). For most of our objects, however, we do not have spectroscopic redshifts and do not know the absolute magnitudes. This can be problematic because we do not know, for example, if the brighter QSOs are indeed more luminous or simply at the low-redshift end of our redshift range (the distance modulus changes by $\sim$0.5 mag from $z = 2.8$ to 3.4). Furthermore, the luminosity function is known to change over these redshifts, which may skew the apparent magnitude distribution from what is expected at a single redshift.

Our only known quantity is the distribution of *apparent* magnitudes of QSOs in this redshift range. Therefore, we have modeled the expected distribution in QSO apparent magnitudes to compare to the observed distribution. The model distributions are computed in the following way:

1. We allow Φ^*, M^*, and faint-end slope, β, to vary independent of one another. We keep the bright-end slope fixed at $\alpha = -2.85$ as determined by SDSS QSOs (Richards et al. 2006a).
2. For each set of parameters, we compute the apparent magnitude distribution in small redshift intervals.
3. At each redshift, we apply the completeness function as a function of apparent magnitude, $C(r', z)$, computed in § 7.3.1.
4. Finally, we sum up the apparent magnitude distribution in each redshift interval to determine the expected apparent magnitude distribution function over the entire redshift range for each set of QLF parameters.
5. We repeat the above steps three times with different QLF evolution: no evolution, PLE, and pure density evolution (PDE). For the two evolving models, we choose the level of evolution to fit the variation in space density of bright QSOs seen by SDSS ($\sim$40% decrease from $z \sim 2.8$ to 3.5; Richards et al. 2006a).

In addition to the observed apparent magnitude distribution from our sample, we also use the QSO sample of Richards et al. (2006a) from the SDSS Data Release 3. We only use the QSOs with $2.9 < z < 3.5$ and use the completeness for each QSO derived in Richards et al. (2006a).

The apparent magnitude distribution function gives the relative probability of finding a QSO with a given magnitude from

TABLE 9
TABULATED LUMINOSITY FUNCTION

r' (Vega)	M(1450 Å) (AB)	n	Completeness	$z_{\rm eff}$	$V_{\rm eff}$ (10^7 Mpc^3)	Φ (10^7 mag^{-1} Mpc^{-3})
18.25	−27.11	0	1.00	3.22	7.87	<0.47
18.75	−26.61	0	1.00	3.22	7.87	<0.47
19.25	−26.11	7	1.00	3.22	7.87	$1.78^{+1.0}_{-0.7}$
19.75	−25.61	5	1.00	3.22	7.87	$1.27^{+0.9}_{-0.5}$
20.25	−25.11	12	0.99	3.22	7.83	$3.07^{+1.2}_{-0.9}$
20.75	−24.61	20	0.98	3.21	7.73	$5.38^{+1.5}_{-1.2}$
21.25	−24.11	25	0.86	3.18	6.77	$7.38^{+1.8}_{-1.5}$
21.75	−23.61	31	0.74	3.15	5.82	$10.66^{+2.3}_{-1.9}$

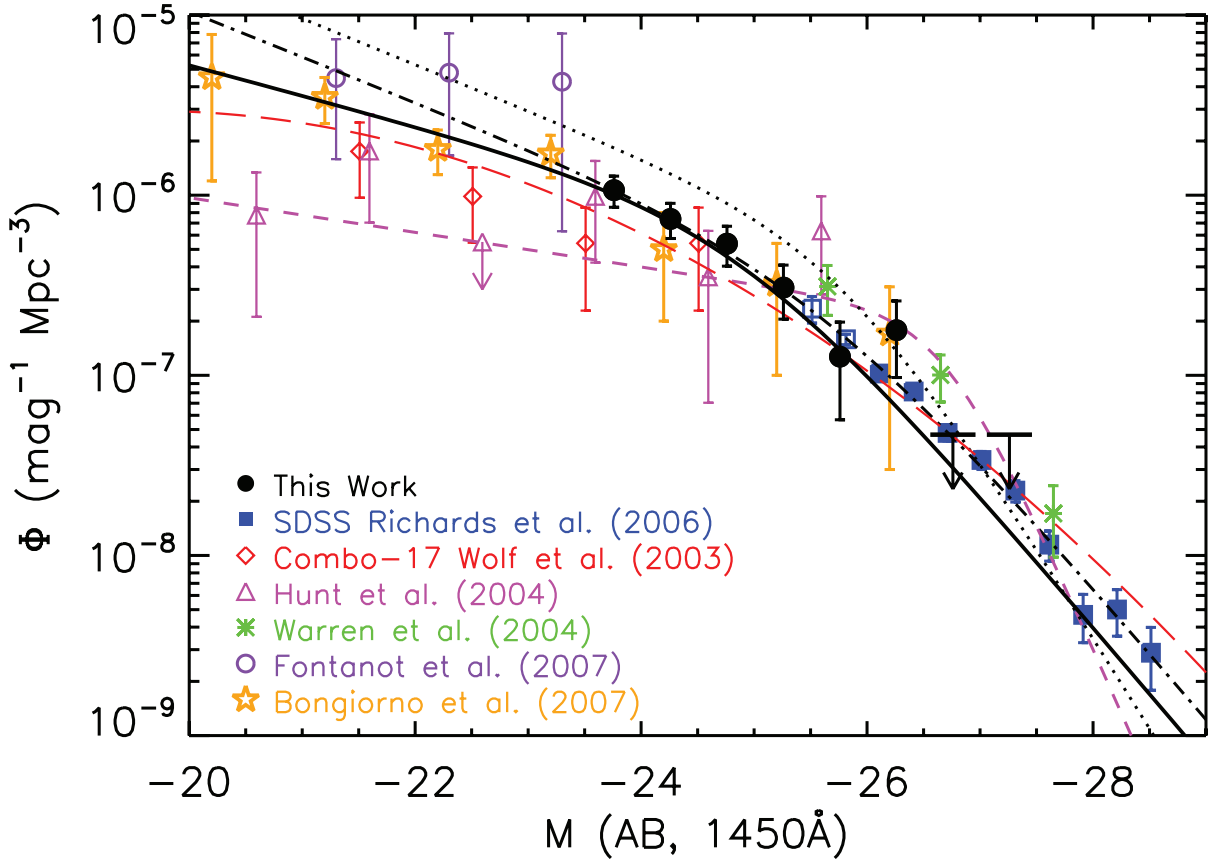

FIG. 16.—The $z \sim 3.2$ QLF. The binned data are plotted from this work (*black circles and black arrows for upper limits*), SDSS (Richards et al. 2006a; *blue squares*), COMBO-17 (Wolf et al. 2003; *red diamonds*), H04 (*cyan triangles*), WHO (Warren et al. 1994; *green asterisks*), Fontanot et al. (2007; *open circles*), and Bongiorno et al. (2007; *orange stars*). Filled symbols were used in the fitting of the QLF. Also plotted are the fitted QLFs using the binned data (*dot-dashed line*), the maximum likelihood fit with PLE (*solid line*), and the QLFs of Pei (1995; *dotted line*), H04 (*magenta short-dashed line*), and Wolf et al. (2003; *red long-dashed line*).

TABLE 10

PARAMETERS FOR DOUBLE POWER-LAW LUMINOSITY FUNCTION

Data	α	β	M^*_{1450} (AB)	Φ^* (10^{-7} mag^{-1} Mpc^{-3})	χ^2	ν[a]
Binned QLF						
SWIRE only	−3.53 (2.9)	−1.66 (0.88)	−25.8 (2.3)	3.5 (11.0)	2.4	3
SWIRE only (fixed α)	[−2.85]	−1.29 (0.85)	−24.8 (1.1)	10.4 (12.0)	2.5	4
SWIRE+SDSS	−3.47 (0.58)	−1.98 (0.17)	−27.1 (0.7)	0.57 (0.65)	9.9	12
SWIRE+SDSS (fixed α)	[−2.85]	−1.62 (0.19)	−25.6 (0.3)	4.53 (2.0)	11.3	13
Maximum Likelihood Fit						
SWIRE only (fixed α, no evolution)	[−2.85]	−1.26 (0.21)	−25.0 (0.30)	9.0 (3.0)	...	...
[PDE $(1+z)^{-3}$]	[−2.85]	−1.22 (0.22)	−25.0 (0.29)	9.3 (2.9)	...	...
(PLE)	[−2.85]	−1.25 (0.21)	−25.0 (0.30)	9.2 (2.9)	...	...
SWIRE+SDSS (fixed α, no evolution)	[−2.85]	−1.43 (0.15)	−24.9 (0.15)	8.5 (2.0)	...	...
[PDE $(1+z)^{-3}$]	[−2.85]	−1.41 (0.15)	−24.9 (0.15)	8.6 (1.9)	...	...
(PLE)	[−2.85]	−1.42 (0.15)	−24.9 (0.15)	8.6 (1.8)	...	...
Previous Studies						
H04	−4.56 (0.51)	−1.24 (0.07)	−26.7	2.4	...	...
Pei (1995)	−3.52 (0.11)	−1.64 (0.18)	−25.8 (0.25)	6.1 (2.5)	...	...
Bongiorno et al. (2007)	−3.0	−1.38	−25.7	9.8	...	...

NOTES.—The binned QLF assumes that all QSOs are at $z = 3.2$, whereas the maximum likelihood values are from fits to the apparent magnitude distribution. Values in parentheses denote 1 σ errors, and values in square brackets denote fixed parameters. The maximum likelihood fits that include QLF evolution (both PDE and PLE) are not significantly different from the no-evolution parameters. Listed at the bottom are estimates from previous work.

the whole sample. We compute the likelihood that a given parameter set adequately describes the data as the product of the values of the apparent magnitude distribution function for all of the QSO r' magnitudes in our sample (Marshall et al. 1983). We then find the set of parameters that maximizes this likelihood. The best-fit model parameters are given in Table 10. The maximum likelihood fit gives a somewhat shallower faint-end slope, $\beta = -1.42 \pm 0.15$, and a similar location of the break and agrees within $\sim 1\ \sigma$ with the binned QLF when we assumed that all QSOs were at $z = 3.2$. The apparent magnitude distributions that included evolution in the QLF (both PLE and PDE) produce best-fit parameters that were not significantly different from the no-evolution fits because there is little evolution over such a small redshift range. We choose to use the PLE model, with $\beta = -1.42 \pm 0.15$, in the subsequent analysis.

9. COMPARISON WITH PREVIOUS LUMINOSITY FUNCTIONS

Plotted in Figure 16 are three previously determined luminosity functions at $z \sim 3$. Pei (1995) compiled several QSO samples to produce a QLF and its evolution between $0 < z < 4.5$. A constant QLF shape was assumed and fitted with PLE. Unfortunately, most of the high-redshift QSOs are very luminous, so the faint-end slope is mostly determined by lower redshift QSOs. As seen in Figure 16, the Pei (1995) QLF has a steeper faint-end slope, $\beta = -1.6$, and lies above our QLF determination until $M^*_{1450} < -26$, where it passes through the SDSS data points. We believe that this discrepancy is caused by the assumption of a constant QLF shape. The Pei (1995) QLF shape was determined mostly by QSOs at $z < 3$ and normalized to the bright QSOs at high redshift. Because the bright-end slope at $z > 3$ is getting shallower (Richards et al. 2006a), this has caused a significant overestimate of the space densities of faint QSOs. In fact, all previous QLF estimates at high redshift that assume a shape derived at low redshift and normalize using bright QSOs will overestimate the number of faint QSOs at $z > 3$. At $z \sim 3$, this results in a factor of ~ 2 overestimate, but it will get worse at higher redshift as the bright-end slope is measured to get even shallower at $3 < z < 5$.

The H04 QLF, although measured with a much smaller sample, shows a very shallow faint-end slope and a steep bright-end slope, resulting in a very prominent break. Our QLF has a significantly shallower bright-end slope and a steeper faint-end slope. The space densities of our faintest QSOs are about twice that of H04 and predict 2–3 times more QSOs between $-24 < M_{1450} < 20$.

H04 threw out most of their AGN sample (16 of 29) because the emission-line widths were less than 2000 km s^{-1}. These narrow-line AGNs are, on average, 1 mag fainter than the broad-line sample. Therefore, if these were included, they would have added significantly to the faint-end counts, resulting in a steeper faint-end slope. We cannot discriminate between different types of AGNs in our sample, since we only have spectra for 10 objects (9 of 10 have FWHM > 2000 km s^{-1}). However, narrow-line AGNs (i.e., FWHM < 2000 km s^{-1}) may explain at least part of the discrepancy in our faint-end slopes.

Recent surveys of X-ray–selected AGNs have also concluded that the faint-end slope gets shallower at higher redshift (Ueda et al. 2003; Hasinger et al. 2005). The Hasinger et al. (2005) sample overlaps our redshift range but differs from ours in the same way as H04, as it is a soft X-ray–selected type I AGN sample. If the difference between the H04 and Hasinger et al. (2005) luminosity functions and our QLF is attributed to increasing numbers of moderately obscured AGNs at fainter rest-frame UV luminosities (as suggested by Ueda et al. 2003), then we would expect to see increasing numbers of QSOs with redder UV spectral slopes and higher $L_{\rm IR}/L_{\rm UV}$ ratios among faint QSOs. Indeed, Figure 11 shows a population of $r' > 21$ QSOs that are redder, in both $r' - [4.5]$ and $r' - [24]$, than any at $r' < 21$, which may not be included in the H04 or Hasinger et al. (2005) LFs.

A recent optical/X-ray search for faint AGNs at $3.1 < z < 5.2$ by Fontanot et al. (2007) finds relatively large space densities, requiring a steep faint-end slope, $\beta = -1.71 \pm 0.41$. Although the errors are large, this rules out a significantly shallower faint-end slope at $z > 3$ and agrees, within $1\ \sigma$, with our fit. In their study, only 18% (2/11) of AGNs have narrow lines. Therefore, the fraction of narrow-line to broad-line AGNs is too small to completely explain the discrepancy between the shallow faint-end slope of H04 and the steep faint-end slope found in this study and in Fontanot et al. (2007).

The COMBO-17 (Wolf et al. 2003) and VVDS (Bongiorno et al. 2007) QLFs are both consistent with our QLF, within errors. Both of these surveys did not require any optical color or morphological criteria, yet they still agree with our numbers. Both the Wolf et al. (2003) and Bongiorno et al. (2007) samples are larger than ours (192 and 130, respectively), but the QSOs are spread out over all redshifts ($0 < z < 5$) so they have 5–10 times fewer QSOs in this redshift range.

10. QSO CONTRIBUTION TO H I IONIZING FLUX AT $z \sim 3.2$

With this new determination of the QLF, we can simply integrate $\Phi(L)$ given in equation (1) to determine the specific luminosity density (at $\lambda = 1450$ Å) of QSOs at $z \sim 3.2$,

$$\epsilon = \int \Phi(L) L\, dL. \tag{10}$$

Integrating from $-30 < M_{1450} < -20$ (43.96 ergs s^{-1} $<$ $\log L_{1450} < 47.96$ ergs s^{-1}), we derive a value for the specific luminosity density, $\epsilon_{1450} = 7.3 \times 10^{24}$ ergs s^{-1} Hz^{-1} h Mpc^{-3}. This is comparable to the values derived from the H04 QLF (7.1×10^{24}) and significantly lower than the value from the Pei (1995) QLF (1.4×10^{25}) when correcting for different cosmologies. Although our QLF determination predicts more integrated UV flux from faint QSOs than that of H04, our M^* is more than 1.5 mag fainter. These two effects essentially cancel out to produce similar luminosity densities.

We can now determine the photoionization rate

$$\Gamma = \int_{\nu_0}^{\infty} d\nu\, 4\pi \frac{J(\nu)}{h\nu} \sigma_{\rm H\,I}(\nu). \tag{11}$$

However, we cannot assume that $J(\nu)$ is the shape of the average QSO SED, since the higher energy photons will be reprocessed by H I and He II, resulting in a higher value for Γ. Haardt & Madau (1996) have modeled this reprocessing in a "clumpy" IGM to determine the effect on the H I photoionization by QSOs. This correctly includes H I clouds as sources of ionizing photons, as well as sinks, and increases Γ by $\sim 40\%$ at $z \sim 3$. We multiply ϵ_{1450} by the ratio of $f_{912}/f_{1450} = 0.58$ in our template and convert to a *proper* volume emissivity at $z = 3.2$ to directly compare with the ϵ_Q calculated by Haardt & Madau (1996) and how it scales with the photoionization rate, $\Gamma_{\rm H\,I}$, and the ionizing intensity at the Lyman limit, J_{912}. It should be stated that the scaling relations from ϵ_Q to J_{912} and $\Gamma_{\rm H\,I}$ are dependent on the value of ϵ_Q itself, as this will effect the ionization levels of the surrounding medium. However, this is a secondary effect, and our ϵ_Q is within $\sim 50\%$ of the Haardt & Madau (1996) value so we do not expect this to be a large effect on the scaling relations.

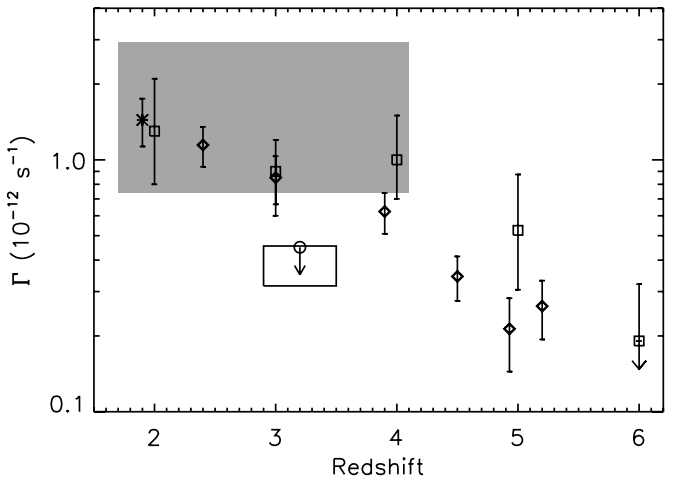

FIG. 17.—H I photoionization rate per atom (in units of 1×10^{-12} s^{-1}) vs. redshift. Estimates of the total photoionization rate of the IGM are plotted as asterisks (Tytler et al. 2004), diamonds (McDonald & Miralda-Escudé 2001), and squares (Bolton et al. 2005; Bolton & Haehnelt 2007). The shaded region is the photoionization rate determined by Scott et al. (2000) adjusted to our cosmology (decrease of 31%) as stated in Scott et al. (2002). The open circle is the H04 determination of the QSO contribution at $z \sim 3$. The black square encompasses the redshift range and plausible limits of the QSO contribution to H I photoionization from our sample. The lower and upper bounds are determined by integrating the QLF to $R < 22$ ($M_{1450} < -23.5$) and $R < 25.5$ ($M_{1450} < -20$), respectively.

We get values of $\Gamma_{\rm H\,I} \sim 4.5 \times 10^{-13}$ s^{-1} and $J_{912} = 1.5 \times 10^{-22}$ ergs s^{-1} cm^{-2} Hz^{-1} sr^{-1}. As pointed out by H04, these should be taken as upper limits as it assumes that all ionizing photons escape from QSOs of all luminosities, although this is not at all clear for lower luminosity AGNs.

It is interesting to compare the H I photoionization rate from QSOs with that from star-forming galaxies (LBGs at these redshifts). Unfortunately, it is difficult to determine the photoionization rate from LBGs, since their photoionizing SEDs are difficult to directly detect and are sensitive to parameters with large uncertainties: dust reddening, initial mass function, starburst age, metallicity, and the escape fraction of ionizing photons, $f_{\rm esc}$ (Steidel et al. 2001; Shapley et al. 2006; Siana et al. 2007).

It is possible, however, to address this question indirectly if the *total* ionizing background (QSOs+galaxies) is accurately determined. Several groups have made these measurements by measuring the mean transmission of QSO UV flux through the Lyα forest (McDonald & Miralda-Escudé 2001; Tytler et al. 2004; Bolton et al. 2005; Bolton & Haehnelt 2007; Becker et al. 2007), or by measuring the extent of the proximity effect (Carswell et al. 1982) around high-redshift QSOs (Scott et al. 2000, 2002). Figure 17 shows the current estimates for the total photoionization rate at high redshift, compared with our estimate of the contribution from QSOs at $z \sim 3.2$. The lower limit to Γ is derived by integrating the QLF between $30 < M_{1450} < 23.5$, the range covered by our survey and SDSS. The upper limit is derived by integrating the QLF 3.5 mag fainter and assumes a 100% escape fraction among these faint QSOs as well. The Scott et al. (2000) value has been scaled (by the value given in Scott et al. 2002) to our assumed cosmology. The McDonald & Miralda-Escudé (2001) values have also been scaled to the same cosmology using equation (3) in their paper.

Although the error bars are large, all of the *total* photoionization measurements are consistent and give a value of $\Gamma \sim 1.0 \times 10^{12}$ s^{-1} at $z = 3$. The contribution from QSOs is less than half of this value. Therefore, it is likely that star-forming galaxies' contribution to the H I photoionization rate is comparable to that of QSOs at $z \sim 3.2$. This is consistent with measurements by Shull et al. (2004), which examine the relative rates of He II and H I photoionization within individual Lyα absorbers at $2.3 < z < 2.9$ to infer the spectral index of background radiation at each location. They conclude that the spectral index varies greatly between absorbers, with significant contribution from "soft" sources that may be starburst galaxies or dust-attenuated AGNs.

Furthermore, recent measurements of the escape fraction, $f_{\rm esc}$, of photoionizing radiation from LBGs also suggest that star formation may significantly contribute to the ionizing background at $z \sim 3$. Steidel et al. (2001) made a composite rest-frame ultraviolet spectrum of 29 LBGs and found that greater than 50% of the photoionizing flux that is not absorbed by dust escapes into the IGM (i.e., *relative* escape fraction $f_{\rm esc,\,rel} > 0.5$). Deeper spectra of 14 $z \sim 3$ LBGs give a smaller value of $f_{\rm esc,\,rel} = 0.14$, but this still gives an ionizing radiation field $J_{900} \sim 2.6 \times 10^{-22}$ ergs s^{-1} cm^{-2} Hz^{-1}, nearly twice the value of our upper limit from QSOs.

11. SUMMARY

We present our method of finding high-redshift ($z > 2.8$) QSOs by identifying a Lyman break in the optical photometry and ensuring red mid-IR ([3.6] − [4.5]) colors indicative of QSOs. The use of only three optical filters allows a search over larger areas in the SWIRE fields as most of the area does not have coverage in four or more bands. The use of only IRAC1 and IRAC2 channels is emphasized as these two bands are a factor of 7 times more sensitive than IRAC3 and IRAC4.

Spectroscopic follow-up of 10 $z \sim 3$ (U-dropout) candidates confirms that all 10 are QSOs between $2.83 < z < 3.44$. Spectroscopy of 10 $z \sim 4$ (g'-dropout) candidates confirmed 7 QSOs with $3.48 < z < 3.88$, 2 galaxies at low redshift ($z = 0.354$ and 0.390), and 1 unconfirmed redshift. We place reliability estimates on our $z \sim 3$ and $z \sim 4$ samples of 100% (>69% 1 σ) and 70^{+16}_{-26} %, respectively. Since we have not spectroscopically confirmed all of our candidates, we only use the more reliable $z \sim 3$ sample for determining a luminosity function.

By using detailed models that include variations in number and column density of LOS H I absorbers, UV spectral slope, emission-line equivalent width, redshift, observed magnitude, and photometric errors, we assess the completeness of the optical color selection. Completeness near the center of the redshift range of our U-dropout selection is 85%–90%. However, our completeness decreases significantly in our faintest magnitudes bins (∼75%), due to the shallow depth of the U-band imaging.

We find 100 $z \sim 3$ QSO candidates with $r' < 22$ over 11.7 deg^2. Through our models of completeness versus redshift, we derive effective volumes for each half-magnitude bin and compute the $z \sim 3$ QLF. When combined with SDSS data, a least-squares fit to a double power law gives a faint-end slope, $\beta = -1.62 \pm 0.19$, and location of the break at $M^* = -25.6$.

Our binned QLF assumes that all of the QSO candidates are at $z = 3.2$, which may skew the fitted parameters because of luminosity function evolution over our redshift range and Eddington bias (Eddington 1913) due to large dispersions in the actual absolute magnitude distribution. Therefore, we have performed a maximum likelihood fit of the *apparent* magnitude distribution of our sample with that inferred from a specific QLF over this redshift range. Our results are slightly different, with a shallower faint-end slope, $\beta = -1.43 \pm 0.15$, and a somewhat fainter break at $M^* = -24.9$. This fit is more accurate as it does not assume that all of the QSOs are at the same redshift.

The fitted slope is consistent, within the errors, with values measured at low redshift ($0.5 < z < 2.0$), $\beta = -1.45$ (Richards et al. 2005), and therefore does not require evolution in the faint-end

slope of the luminosity function. Our QLF predicts significantly more faint QSOs than suggested with initial measurements at $z \sim 3$ (H04). Although it is difficult to tell with our limited spectroscopic sample, some of the difference between our faint-end slope and that of H04 may be attributed to an increasing number of narrow-line, moderately reddened AGNs at fainter UV luminosities that were excluded from the H04 sample.

The QLF exhibits some curvature at all magnitudes and, because of this, the parameters for a double power-law fit are degenerate. That is, the position of the break, (M^*, Φ^*), can be fitted at different locations along the binned QLF, with appropriate changes in the bright- and faint-end slopes (α, β). This is especially true at high redshift, where the difference between the bright- and faint-end slopes appears to decrease. Therefore, one must be careful when assigning physical significance to the measured values of these parameters when comparing to models.

The QSOs in our sample span the break in the luminosity function ($0.25L^* < L < 4.0L^*$), and thus we measure the space density of QSOs that comprise the majority (55%) of the QSO UV luminosity density at these redshifts. When combined with the SDSS sample, this percentage is more than 70%. Therefore, large extrapolations are not required to estimate the effects of undetected QSOs. The integrated UV luminosity density at $z \sim 3.2$ is $\epsilon_{1450} = 7.3 \times 10^{24}$ ergs s^{-1} Hz^{-1} h Mpc^{-3}. Using the scaling relation derived by Haardt & Madau (1996), we infer a maximum H I photoionization rate by QSOs, $\Gamma = 4.5 \times 10^{-13}$ s^{-1}. This is about 50% of the *total* IGM H I photoionization rate at $z = 3$, requiring comparable ionizing flux from either starburst galaxies or redder AGNs that lie outside our color criteria.

This work is based on observations made with the *Spitzer Space Telescope*, which is operated by the Jet Propulsion Laboratory, California Institute of Technology under a contract with NASA. Support for this work, part of the *Spitzer Space Telescope* Legacy Science Program, was provided by NASA through an award issued by JPL/Caltech, under NASA contract 1407.

Based in part on observations obtained at the Hale Telescope, Palomar Observatory as part of a continuing collaboration between the California Institute of Technology, NASA/JPL, and Cornell University.

Based in part on data made publicly available through the Isaac Newton Group's Wide Field Camera Survey Programme. The Isaac Newton Telescope is operated on the island of La Palma by the Isaac Newton Group in the Spanish Observatorio del Canarias.

This publication makes use of data products from the Two Micron All Sky Survey, which is a joint project of the University of Massachusetts and the Infrared Processing and Analysis Center/California Institute of Technology, funded by the National Aeronautics and Space Administration and the National Science Foundation.

Facilities: Spitzer(IRAC, MIPS)

REFERENCES

Barger, A. J., Cowie, L. L., Mushotzky, R. F., Yang, Y., Wang, W.-H., Steffen, A. T., & Capak, P. 2005, AJ, 129, 578
Barvainis, R. 1987, ApJ, 320, 537
Bechtold, J. 1994, ApJS, 91, 1
Becker, G. D., Rauch, M., & Sargent, W. L. W. 2007, ApJ, 662, 72
Beichman, C. A., Cutri, R., Jarrett, T., Stiening, R., & Skrutskie, M. 2003, AJ, 125, 2521
Bershady, M. A., Charlton, J. C., & Geoffroy, J. M. 1999, ApJ, 518, 103
Bertin, E., & Arnouts, S. 1996, A&AS, 117, 393
Bolton, J. S., & Haehnelt, M. G. 2007, MNRAS, 382, 325
Bolton, J. S., Haehnelt, M. G., Viel, M., & Springel, V. 2005, MNRAS, 357, 1178
Bongiorno, A., et al. 2007, A&A, 472, 443
Boyle, B. J., Shanks, T., Croom, S. M., Smith, R. J., Miller, L., Loaring, N., & Heymans, C. 2000, MNRAS, 317, 1014
Boyle, B. J., Shanks, T., & Peterson, B. A. 1988, MNRAS, 235, 935
Brown, M. J. I., et al. 2006, ApJ, 638, 88
Carswell, R. F., Whelan, J. A. J., Smith, M. G., Boksenberg, A., & Tytler, D. 1982, MNRAS, 198, 91
Croom, S. M., Smith, R. J., Boyle, B. J., Shanks, T., Miller, L., Outram, P. J., & Loaring, N. S. 2004, MNRAS, 349, 1397
Dunlop, J. S., & Peacock, J. A. 1990, MNRAS, 247, 19
Eddington, A. S. 1913, MNRAS, 73, 359
Elvis, M., et al. 1994, ApJS, 95, 1
Fan, X., et al. 2001, AJ, 121, 54
Fazio, et al. 2004, ApJS, 154, 10
Fontanot, F., Cristiani, S., Monaco, P., Nonino, M., Vanzella, E., Brandt, W. N., Grazian, A., & Mao, J. 2007, A&A, 461, 39
Francis, P. J. 1996, Publ. Astron. Soc. Australia, 13, 212
Giavalisco, M. 2002, ARA&A, 40, 579
Gonzalez-Solares, E. A., et al. 2005, MNRAS, 358, 333
Gunn, J. E., & Stryker, L. L. 1983, ApJS, 52, 121
Haardt, F., & Madau, P. 1996, ApJ, 461, 20
Haiman, Z., & Menou, K. 2000, ApJ, 531, 42
Hartwick, F. D. A., & Schade, D. 1990, ARA&A, 28, 437
Hasinger, G., Miyaji, T., & Schmidt, M. 2005, A&A, 441, 417
Hatziminaoglou, E., et al. 2005, AJ, 129, 1198
Heisler, J., & Ostriker, J. P. 1988, ApJ, 325, 103
Hogan, C. J., Anderson, S. F., & Rugers, M. H. 1997, AJ, 113, 1495
Hopkins, P. F., Hernquist, L., Cox, T. J., Robertson, B., Di Matteo, T., & Springel, V. 2006, ApJ, 639, 700
Hunt, M. P., Steidel, C. C., Adelberger, K. L., & Shapley, A. E. 2004, ApJ, 605, 625 (H04)
Imanishi, M., & Dudley, C. C. 2000, ApJ, 545, 701
Irwin, M., & Lewis, J. 2001, NewA Rev., 45, 105
Irwin, M., McMahon, R. G., & Hazard, C. 1991, in ASP Conf. Ser. 21, The Space Distribution of Quasars, ed. D. Crampton (San Francisco: ASP), 117
Jakobsen, P., Boksenberg, A., Deharveng, J. M., Greenfield, P., Jedrzejewski, R., & Paresce, F. 1994, Nature, 370, 35
Kauffmann, G., & Haehnelt, M. 2000, MNRAS, 311, 576
Kennefick, J. D., Djorgovski, S. G., & de Carvalho, R. R. 1995, AJ, 110, 2553
Kim, T.-S., Hu, E. M., Cowie, L. L., & Songaila, A. 1997, AJ, 114, 1
Koo, D. C., & Kron, R. G. 1988, ApJ, 325, 92
Kormendy, J., & Richstone, D. 1995, ARA&A, 33, 581
Lacy, M., et al. 2004, ApJS, 154, 166
Lonsdale, C. J., et al. 2003, PASP, 115, 897
Madau, P. 1995, ApJ, 441, 18
Madau, P., Ferguson, H. C., Dickinson, M. E., Giavalisco, M., Steidel, C. C., & Fruchter, A. 1996, MNRAS, 283, 1388
Madau, P., Haardt, F., & Rees, M. J. 1999, ApJ, 514, 648
Magorrian, J., et al. 1998, AJ, 115, 2285
Marshall, H. L. 1985, ApJ, 299, 109
Marshall, H. L., Tananbaum, H., Avni, Y., & Zamorani, G. 1983, ApJ, 269, 35
Massey, P., Strobel, K., Barnes, J. V., & Anderson, E. 1988, ApJ, 328, 315
McDonald, P., & Miralda-Escudé, J. 2001, ApJ, 549, L11
McMahon, R. G., Walton, N. A., Irwin, M. J., Lewis, J. R., Bunclark, P. S., & Jones, D. H. 2001, NewA Rev., 45, 97
Oke, J. B., et al. 1995, PASP, 107, 375
Pei, Y. C. 1995, ApJ, 438, 623
Reimers, D., Kohler, S., Wisotzki, L., Groote, D., Rodriguez-Pascual, P., & Wamsteker, W. 1997, A&A, 327, 890
Richards, G. T., et al. 2002, AJ, 123, 2945
———. 2005, MNRAS, 360, 839
———. 2006a, AJ, 131, 2766
———. 2006b, ApJS, 166, 470
Rieke, G. H., et al. 2004, ApJS, 154, 25
Sanders, D. B., Phinney, E. S., Neugebauer, G., Soifer, B. T., & Matthews, K. 1989, ApJ, 347, 29
Schmidt, M. 1968, ApJ, 151, 393
Schmidt, M., & Green, R. F. 1983, ApJ, 269, 352
Schmidt, M., Schneider, D. P., & Gunn, J. E. 1995, AJ, 110, 68
Schneider, D. P., et al. 2005, AJ, 130, 367
Scott, J., Bechtold, J., Dobrzycki, A., & Kulkarni, V. P. 2000, ApJS, 130, 67
Scott, J., Bechtold, J., Morita, M., Dobrzycki, A., & Kulkarni, V. P. 2002, ApJ, 571, 665

Shapley, A. E., Steidel, C. C., Pettini, M., Adelberger, K. L., & Erb, D. K. 2006, ApJ, 651, 688
Shull, J. M., Tumlinson, J., Giroux, M. L., Kriss, G. A., & Reimers, D. 2004, ApJ, 600, 570
Siana, B., et al. 2007, ApJ, 668, 62
Silva, L., Granato, G. L., Bressan, A., & Danese, L. 1998, ApJ, 509, 103
Skrutskie, M. F., et al. 2006, AJ, 131, 1163
Small, T. A., & Blandford, R. D. 1992, MNRAS, 259, 725
Sokasian, A., Abel, T., & Hernquist, L. 2002, MNRAS, 332, 601
Steidel, C. C., Giavalisco, M., Pettini, M., Dickinson, M., & Adelberger, K. L. 1996, ApJ, 462, L17
Steidel, C. C., Pettini, M., & Adelberger, K. L. 2001, ApJ, 546, 665
Steidel, C. C., Shapley, A. E., Pettini, M., Adelberger, K. L., Erb, D. K., Reddy, N. A., & Hunt, M. P. 2004, ApJ, 604, 534
Stern, D., et al. 2005, ApJ, 631, 163
Storrie-Lombardi, L. J., McMahon, R. G., Irwin, M. J., & Hazard, C. 1994, ApJ, 427, L13
Storrie-Lombardi, L. J., & Wolfe, A. M. 2000, ApJ, 543, 552
Surace, J. A., et al. 2005, ApJ, 631, 163
Telfer, R. C., Zheng, W., Kriss, G. A., & Davidsen, A. F. 2002, ApJ, 565, 773
Tytler, D., et al. 2004, ApJ, 617, 1
Ueda, Y., Akiyama, M., Ohta, K., & Miyaji, T. 2003, ApJ, 598, 886
Vanden Berk, D. E., et al. 2001, AJ, 122, 549
———. 2004, ApJ, 601, 692
Warren, S. J., Hewett, P. C., & Osmer, P. S. 1994, ApJ, 421, 412
Werner, M. W., et al. 2004, ApJS, 154, 1
Weymann, R. J., et al. 1998, ApJ, 506, 1
Wolf, C., Wisotzki, L., Borch, A., Dye, S., Kleinheinrich, M., & Meisenheimer, K. 2003, A&A, 408, 499
York, D. G., et al. 2000, AJ, 120, 1579